

New insights on the fault structure of a geothermal testbed and the associated seismicity based on active seismic tomography

Miriam Larissa Schwarz¹, Hansruedi Maurer², Anne Obermann^{1,2}, Paul Antony Selvadurai¹, Alexis Shakas², Stefan Wiemer¹, and Domenico Giardini²

¹Swiss Seismological Service, ETH Zürich, Sonneggstrasse 5, CH-8092 Zürich

²Institute of Geophysics, ETH Zürich, Sonneggstrasse 5, CH-8092 Zürich

Correspondence: Miriam Larissa Schwarz (miriam.schwarz@sed.ethz.ch)

Abstract. To obtain reliable high-resolution subsurface images in the geothermal testbed of the Bedretto Underground Laboratory for Geosciences and Geoenergies (BedrettoLab), we applied fat ray travel time tomography with the aim of better understanding the relationship between structural features and the seismicity induced by hydraulic stimulation tests. For the computation a 3D velocity model, we utilized eight boreholes, which provided us with a large data set comprising 42'843 manually picked first breaks. Our results demonstrate that the fat ray approach offers improved image quality compared to traditional ray-based methods. The 3D model was further validated using ground-truth information from wireline logs and geological observations. We successfully imaged a major fault zone (MFZ) that exhibits a complex structure including considerable heterogeneity. Relocation of passive seismic events generated during hydraulic stimulations indicates that the 3D velocity model has only a minor influence on hypocentral parameters. However, comparing a selection of well-constrained seismic events with the velocity structures revealed a remarkable spatial correlation. Most events occurred in regions of intermediate and slightly decreased seismic velocities, thereby avoiding both high- and very low-velocity zones. Based on small-scale laboratory studies, we speculate that these observations can be explained by the presence of stress gradients in the intermediate-velocity zones.

Copyright statement.

1 Introduction

Energy production from sustainable resources is a key challenge of this century. Geothermal energy is recognized as a viable option. In particular, so-called “enhanced geothermal systems” (EGS) may have the potential to produce electrical energy at affordable costs (e.g. Olasolo et al. (2016); Hirschberg et al. (2015)). Key challenges include establishing sustainable flow rates, while controlling the associated induced seismicity Zang et al. (2024). Examples of EGS projects that had to be stopped due to high seismicity include, for example, Basel (Edwards et al., 2015) and Pohang (Ellsworth et al., 2019). These problems are closely linked with the often poorly known fracture network of the reservoir. Therefore, several initiatives have been established to better characterize relevant host rock structures with near-field observations and well-monitored stimulation experiments. (Amann et al., 2018; Obermann et al., 2024; Kneafsey et al., 2025).

Seismic studies can offer powerful tools for imaging key structures, such as permeable fracture zones, which are the main targets of EGS investigations. They can be applied during an initial characterization phase or during the stimulation phase.

25 Generally, it can be distinguished by passive and active seismic techniques. Passive techniques do not require actively fired seismic sources. Instead, either information contained in the ambient noise is exploited (e.g., Obermann and Hillers (2019)) or recordings from the induced seismicity are analyzed. For example, Charl  ty et al. (2006) conducted a 4D tomographic study using induced seismicity at the Soultz-sous-For  ts Hot Dry Rock site in France, that is, temporal 3D seismic velocity changes were computed.

30 Active seismic methods can generally be subdivided in reflection and refraction imaging and transmission tomography. Reflection and refraction imaging can be carried out either from the surface, or surface-to-borehole configurations - also referred as vertical seismic profiling (VSP) techniques. In geothermal applications, VSP is particularly popular. For example, Nakata et al. (2023) used VSP data for reflection imaging of faults and fractures at the geothermal test site FORGE, Utah, U.S.A.. It is also possible to combine induced seismicity methods with reflection imaging. Block et al. (1994) applied a joint hypocenter-

35 velocity inversion using induced seismicity from Hot dry rock (HDR) experiments at Los Alamos National Laboratory, New Mexico to gain a 3D velocity model. Nakagome et al. (1998) used a seismic reflection survey together with vertical seismic profiling (VSP) to image the fractured reservoir in the Kakkonda geothermal field (Japan). Place et al. (2011) employed induced seismicity and VSP data to map fractures in Soultz-Sous-F  rets (France). Transmission tomography primarily makes use of direct, diving or refracted waves traveling from sources to the receivers. It can be either applied from the surface (e.g.,

40 Zelt and Barton (1998); Lanz et al. (1998); Heincke et al. (2006)), or between boreholes (e.g., Pratt and Worthington (1988); Maurer and Green (1997)). Here, the travel times of the first arriving waves are exploited to establish 2D or 3D distributions of the seismic velocities. Alternatively, the first break amplitudes can be used to compute attenuation models (e.g., Holliger et al. (2001)). All these studies provided useful information for a better understanding of the subsurface structures.

Since seismic waves travel in a heterogeneous medium along complicated wave paths, 2D tomographic investigations suffer

45 from inherent limitations, resulting from the assumption that the wave paths lie exclusively within the tomographic (2D) plane. Therefore, 3D investigations should be carried out, when complex subsurface structures are expected. This can be achieved quite easily with surface-based investigations, because the sources and receivers can be well distributed over the earth's surface, which results in a good seismic ray coverage of the structures of interest, given that acquisition offset is large enough. In the case of crosshole investigations, this is often a problem, because there are rarely enough boreholes available that allow a good

50 ray coverage of the subsurface region of interest. Therefore, 3D crosshole tomography experiments are very rare, which is unfortunate, because they can potentially offer very relevant and unique subsurface information. The problem of poor ray coverage can be, at least partially, alleviated with the concept of fat rays, where it is assumed that seismic waves are not traveling along infinitesimally thin rays, but within "fat rays", whose thickness is governed by the dominant frequencies of the seismic waves (e.g. Woodward, 1992). Initial concepts were provided by Woodward (1992), and fat ray approaches were implemented

55 for local earthquake tomography (Husen and Kissling, 2001) and active seismic experiments (Jordi et al., 2016). We have applied these concepts in the framework of the host rock characterization in the Bedretto Lab (Ma et al., 2022; Plenkens et al., 2022). As discussed in more detail in Section 2, this is a unique research environment including a geothermal

testbed, which mimics a realistic reservoir structure in crystalline rocks. For example, it includes important structures, such as a major fault zone (MFZ). In total, nine boreholes were drilled within the geothermal testbed, out of which eight were available for active seismic measurements. This offered exciting opportunities for testing the benefits and limitations of 3D travel time tomography. ~~As described in this contribution,~~ several active seismic crosshole measurements were carried out, and they were analyzed with a fat ray tomography approach. The primary aim of our study is to image important geological structures, and to better understand the relationship between these structural features and the seismicity, induced by various hydraulic stimulation experiments within the geothermal testbed.

We start with a description of the Bedretto Lab, the embedded geothermal testbed, and we briefly summarize key results from previous investigations in the BedrettoLab. Then, we present our data set, followed by a short description of the methodology employed to establish the 3D velocity models. After the presentation of the tomographic results, we perform a joint interpretation with geological and geophysical add-on data sets that were also acquired at our test site. In particular, we discuss the spatial correlation between passive seismic events and the velocity structures found.

2 Site description

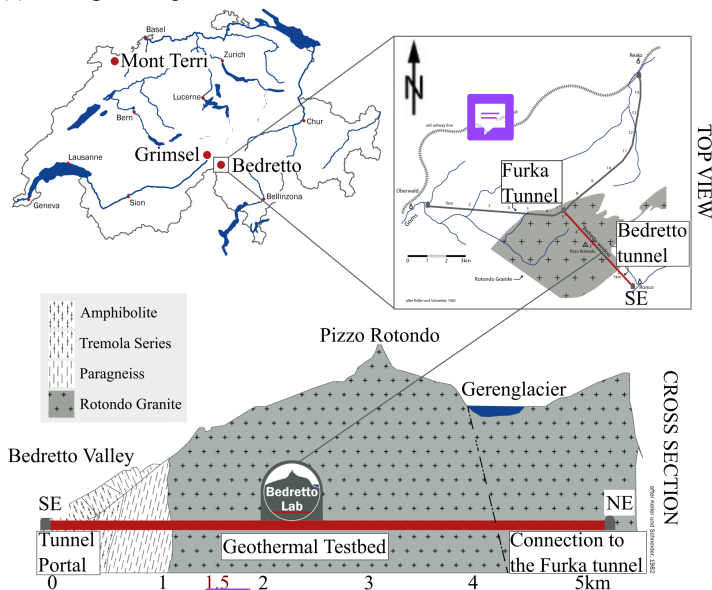
The Bedretto Underground Laboratory for Geosciences and Geoenergies (BULGG or BedrettoLab), operated by ETH Zurich, is located in the central Swiss Alps (Ticino) in a 5.2 kilometres long side tunnel of the Furka railway tunnel (Figure 1a). The BedrettoLab is a unique research facility that provides optimal conditions for conducting experimental research on understanding the responses of the deep underground during hydraulic stimulations. With dimensions at the hectometer scale (hundreds of meters extension), the BedrettoLab closes the gap between the decameter laboratory scale (tens of meters extension, e.g., Grimsel test site (Gischig et al., 2020)) and the reservoir scale (hundreds of meters to kilometers, (Amann et al., 2018)).

The BedrettoLab host rock is composed of mainly granites, which are referred to as the Rotondo Granite. Its intrusion into the Gotthard Massif took place during the late Variscan orogeny (Sergeev et al. (1995)). In general, the Rotondo Granite is homogeneous, that is, it generally exhibits isotropic structures, but at some places, weak signs of metamorphism are observed, (Labhart T, 2005; Lützenkirchen and Loew, 2011). This may have slightly altered the isotropic structures (see also Figure 1b). ~~Indeed,~~ Behnen et al. (2024) identified weak signs of anisotropy near the geothermal testbed, but for the sake of simplicity, we assume an isotropic velocity structure for this study.

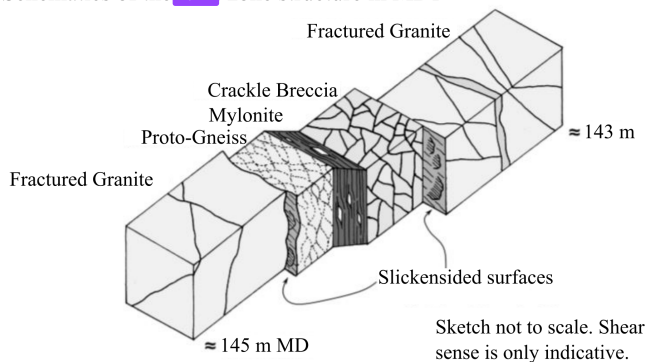
According to the World Stress Map (Heidbach et al., 2018), the main horizontal compressive stresses are oriented in NW-SE direction, but Bröker et al. (2024a) showed that within the BedrettoLab, the orientation of the stress field can exhibit significant variations. Due to the overburden, the principal stress axis can be assumed to be vertical, and a previous study of Meier (2017) revealed that topographic effects can be neglected in the area of the BedrettoLab.

The geothermal testbed is located between tunnel meters 2000 m to 2100 m, measured from the tunnel portal (see Figure 1a)). It has an overburden of about 1030 m, and includes several boreholes, ranging from 250 m to 400 m length. The six monitoring boreholes (MB1, MB3-MB5, MB7, MB8) are equipped with a state-of-the-art monitoring system. This includes seismic sensors (geophones, accelerometers and acoustic emission sensors) as well as active piezoelectric seismic sources. In addition,

(a) Geological map + BedrettoLab



(b) Schematics of the  zone structure in MB1



(c) Boreholes  main axis system and fault zone

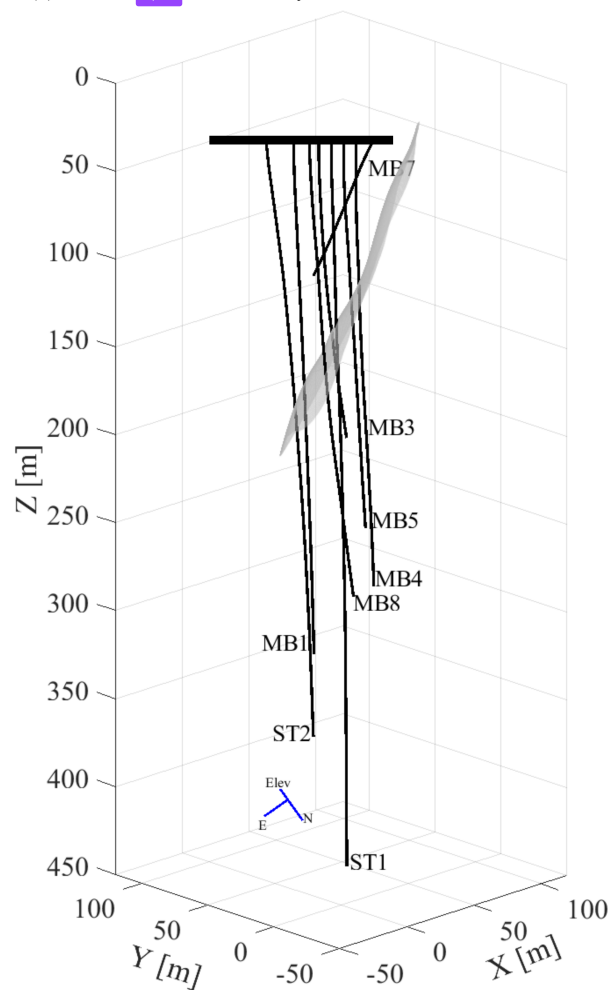


Figure 1. (a) Location and geological map of the BedrettoLab (see also Ceccato et al. (2024) and Rast et al. (2022)). (b) Schematics of the Major Fault Zone (MFZ), as observed in borehole MB1. The MFZ is found between 143 and 145 m depth in this borehole. Fractured Granites surround Porto-Gneiss, Mylonite and Crackle Beccia (figure adjusted from Ma et al. (2022)). (c) Boreholes drilled into the Geothermal Testbed, including six monitoring boreholes (MB1, MB3-MB5, MB7, MB8), one stimulation (ST1) and one extraction (ST2) borehole. Here, the boreholes are shown in the tomography coordinate system, which was used in this paper. The blue arrows show the orientation of the original Bedretto coordinate system with Easting, Northing and Elevation, as used in panel a). Additionally, panel c) depicts the 3D structure of the MFZ (gray surface) as derived by Escallon et al. (2024).

a stimulation (ST1) and an extraction (ST2) borehole were drilled into the testbed. ST1 was equipped with a multi-packer system, with which it was subdivided into 14 intervals (Bröker et al., 2024a). ST2 was kept open for the use of various measurements, for example, active seismic measurements. For more details on the multi-disciplinary monitoring system, we refer to the overview paper of Plenkers et al. (2022).

95 Faults and fractures within the geothermal testbed have been mapped mainly as subvertically dipping, predominantly striking NE-SW to ENE-WSW (Labhart T, 2005; Lützenkirchen and Loew, 2011) and frequently steeply dipping, striking N-S and E-W along the tunnel (Jordan, 2019). Ma et al. (2022) and Bröker et al. (2024b) show detailed maps of fractures along the tunnel, which are based on tunnel wall mapping and borehole logging. The fractures can be divided into four different sets: striking N-S, NE-SW/tunnel perpendicular, E-W, and NW-SE/tunnel parallel.

100 A major fault zone (MFZ) within the geothermal testbed is of particular interest for this paper. It was discovered by previous studies using all available boreholes. This included core analyses as well as acoustic and optic televiewer (ATV/OTV) observations (Ma et al., 2022). A schematic of the MFZ, as observed in borehole MB1, is shown in Figure 1b. It includes Proto-Gneis, Mylonite and Crackle Breccia that surround fractured granites. More details on this structures can be found in Ma et al. (2022), but for the purpose of this paper is primarily important to note that the complexity of the MFZ will represent a challenge for
105 the tomographic imaging. Besides the a priori information, offered by the core and televiewer analyses, we also have access to a 3D image of the MFZ. It was obtained with a borehole radar reflection study (Escallon et al., 2024) , and the 3D surface of the MFZ is shown in gray in Figure 1c.

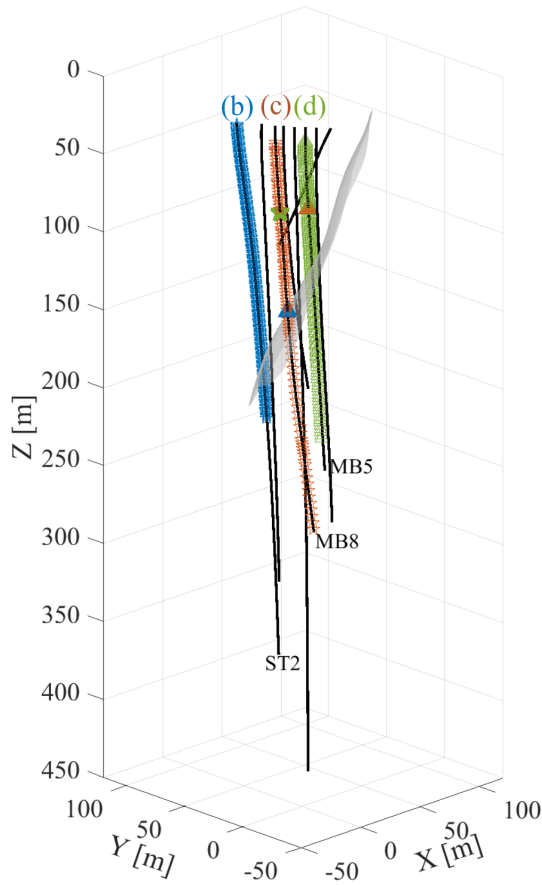
Since we will later relate our tomographic inversions with the seismicity, generated by hydraulic stimulations, it is important to note that the BedrettoLab lies in an area of generally low seismicity (e.g. Diehl et al. (2025), Gischig et al. (2020)). All the
110 seismic events, discussed later in this study, are caused by stimulations within the geothermal testbed, and they are not superimposed by a seismic background activity. Furthermore, it is also important to note that the stress conditions in the BedrettoLab mimic stress conditions of a real geothermal reservoir, but the temperatures are much lower (approx. 18 degrees Celsius, Ma et al. (2022)).

3 Data

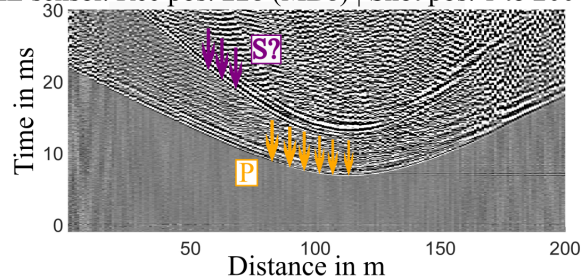
115 ~~Although the geological and geophysical studies discussed in Section 2 provided key information for the characterization of the Geothermal Testbed, it was judged to be necessary to obtain additional volumetric information. This can be obtained from active seismic crosshole measurements.~~ The full active seismic data set, employed in this study, is composed of several independent surveys that were taken at different times from October 2020 to November 2021, depending on when the boreholes were drilled and being available. A detailed overview is given in Table 1. The borehole configuration is shown in Figures 1b
120 and 1c. The spacing of the source varied between 1 m, 2 m, and 5 m for the different surveys and along the borehole depths.

We employed a seismic P-wave sparker source with a dominant frequency band of about 1 to 10 kHz (<https://geotomographie.de>). The first three data sets were recorded on two hydrophone chains with 1 m and 2 m spacing, respectively (Table 1). The

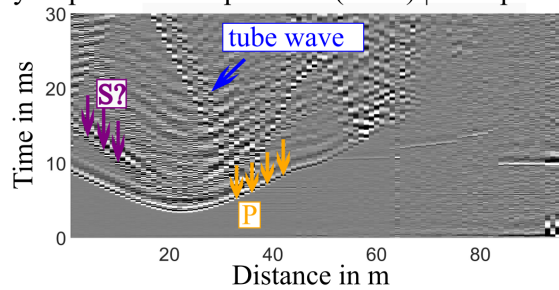
(a) shot and receiver positions



(b) AE sensor. Rec pos: 228 (MB8) | Shot pos: 1 to 200 (ST2)



(c) Hydrophones. Rec pos: 113 (MB5) | Shot pos: 1 to 180 (MB8)



(d) Hydrophones. Shot pos: 38 (MB8) | Rec pos: 70 to 355 (MB5)

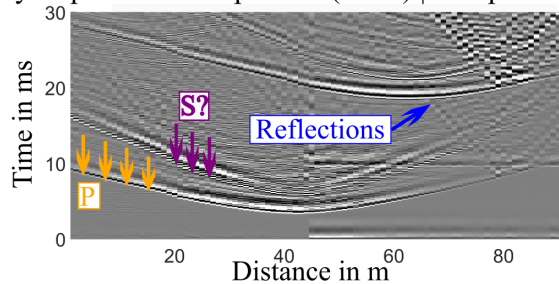


Figure 2. Experimental setup and data examples. a) shows the shot (stars) and receiver (triangles) positions for the waveforms shown in b), c) and d). The gray surface indicates the MFZ as derived by Escallon et al. (2024). b) displays the waveforms recorded by an AE sensors in borehole MB8 (blue triangle) from shots in borehole ST2 (blue stars). c) shows a corresponding receiver gather recorded on a hydrophone in MB5 (brown triangle) and shots in borehole MB8 (brown stars). d) shows a shot gather from a source in MB8 (green star) with hydrophones in MB5 (green triangles). First arrivals for P-wave are indicated with yellow arrows, and examples for reflections and tube wave are indicated with blue arrows. The predicted S-wave arrivals are indicated with purple arrows.

Table 1. Acquisition parameters of the active seismic survey

borehole source	borehole receiver	shot spacing	receiver spacing	sensor	date	number of traces	number of picks
ST1	ST2	2 m	1m/2m	hydrophones	Oct. 2020	15307	7413
MB4	MB1	2 m	1 m	hydrophones	Oct. 2020	5376	3716
MB3	MB4	2 m	1 m	hydrophones	Oct. 2020	3648	1780
MB3	MB1	2 m	1 m	hydrophones	Oct. 2020	1824	1337
MB1	MB4	2 m	1 m	hydrophones	Oct. 2020	2976	1620
MB8	MB7	5 m/2 m	1 m/2 m	hydrophones	June 2021	4840	2476
MB8	MB5	5 m/2 m	1 m/2 m	hydrophones	June 2021	13698	7143
MB5	MB7	5 m/2 m	1 m/2 m	hydrophones	June 2021	6644	4610
MB5	MB8	5 m/2 m	1 m/2 m	hydrophones	June 2021	14562	9437
ST2	MB1	1 m	fixed depth	AE sensors	Nov. 2021	800	179
ST2	MB3	1 m	fixed depth	AE sensors	Nov. 2021	1400	781
ST2	MB4	1 m	fixed depth	AE sensors	Nov. 2021	1200	667
ST2	MB5	1 m	fixed depth	AE sensors	Nov. 2021	800	539
ST2	MB7	1 m	fixed depth	AE sensors	Nov. 2021	200	158
ST2	MB8	1 m	fixed depth	AE sensors	Nov. 2021	1600	987
total number of source points:	649						
total number of receiver points:	962						
total number of traces:	74875						
total number of picks:	42843 (57.2%)						
source type:	P-wave sparker						
sampling frequency							
hydrophones:	48 kHz						
AE sensors:	200 kHz						

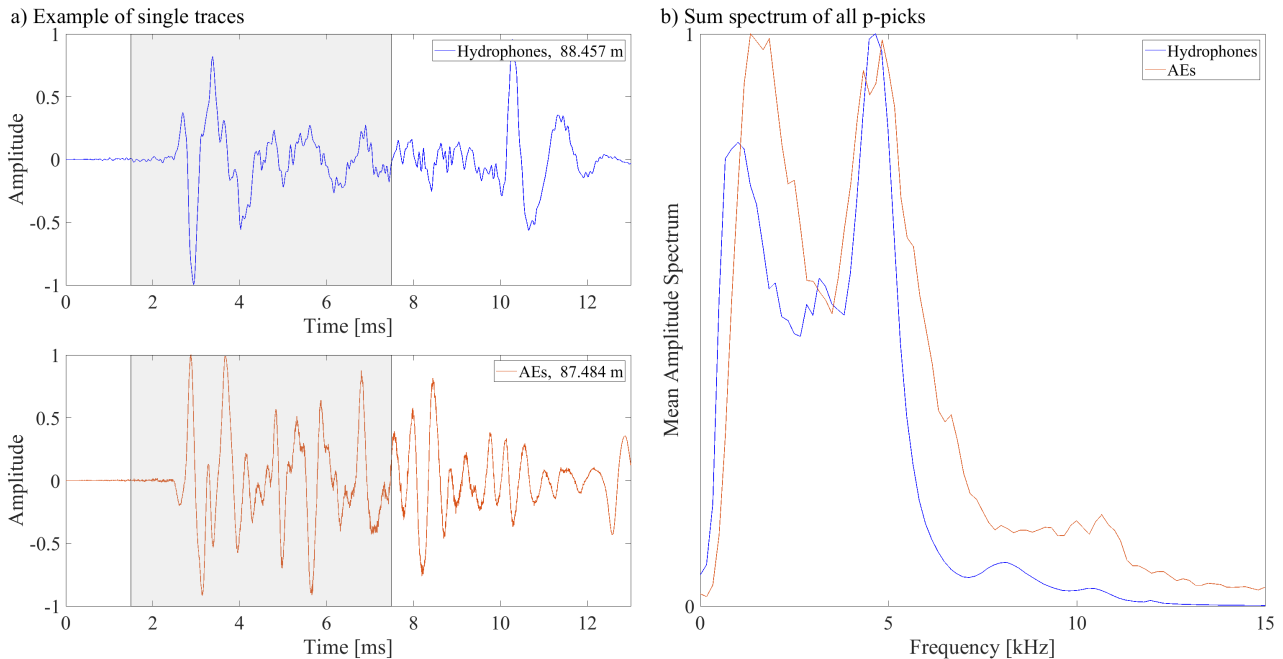


Figure 3. a) Example traces of a hydrophone (top) and an AE sensor (bottom) that were recorded at similar source-receiver offsets. The gray boxes indicates the time window that was used to calculate the sum spectra shown in b) . For visualisation purposes, we normalized the data to the maximum amplitude. b) shows the sum spectra of all traces with a P pick (see main text for further explanations on the computation of the sum spectra).

surveys were designed, such that the receiver/shot spacing is denser around the MFZ and sparser at larger distances away from
 125 it. These surveys were conducted before the instrumentation and cementation of the boreholes. The last survey was carried out in November 2021, after the instrumentation, but prior to stimulation experiments. Permanently installed acoustic emission (AE) sensors were used as receivers, which had to be synchronized with the sparker setup. For each source point and all surveys, the sparker source was fired three times, and the traces were then stacked to enhance the signal-to-noise (SNR) ratio. Overall, we were able to compile a relatively large data set including 42'843 manual P-picks (Table 1) with an average picking
 130 uncertainty of about 0.15 ms. This value was estimated on the basis of visual inspections during the manual picking process. Source-receiver offsets varied between 10 m and 186.5 m. For the manual picking, we employed a **Matlab-based in-house software**.

In Figure 2, we show three examples of shot and receiver gathers. Figure 2a) shows the setting with the source and receiver configurations as well as the MFZ. 2b) displays a receiver gather recorded on the AE sensors (sensor in MB8, sources in ST2),
 135 2c) shows a receiver gather recorded on a hydrophone (sensor in MB5 and receiver in MB8) and 2d) shows a source gather recorded on hydrophones (source position in MB5 and receivers in MB8). The first arrivals of the P-waves, indicated by the yellow arrows, are clearly visible. The P-wave sparker, as the name suggests, is designed to generate primarily seismic P-waves.

S-waves that are visible in the data are therefore most likely converted P-to-S phases, with the conversion likely taking place at the source borehole wall. The S-waves are marked in Figures 2b, c, and d, (~~indicated with~~ purple arrows). They are generally
140 difficult to pick, because they often overlap with scattered parts of the P-waves or with reflected waves. Therefore, we restrict ourselves to the first arriving P waves.

Figure 3a shows example traces from a hydrophone and an AE sensor with a similar source-receiver offset. Both traces show a high signal-to-noise ratio. To further appraise the properties of the seismic waveforms, we computed sum spectra for the hydrophone and AE sensor data. For that purpose, all traces with a P pick were considered. A time window of 6 ms around the
145 first break was considered to calculate the amplitude spectra (gray boxes in Figure 3a). The amplitude spectra of the individual traces were then summed up to obtain the sum spectra.

The frequency content of both sensor types is comparable, with the energy of the first-arriving waves varying between 1 kHz and 7.5 kHz. It should be noted that the sharp decrease below 1 kHz is caused by analog filters of the acquisition systems. Furthermore, it is noteworthy that there is a significant decrease of spectral amplitudes around 3 kHz for both sensor types.
150 One may argue that this feature in the sum spectra is caused by the sensor properties or by the acquisition system. However, the hydrophone and AE sensor data were not only captured by different sensors, but they were also acquired with different acquisition systems. Therefore, it ~~must be concluded~~ that the shape of the sum spectra ~~must be~~ caused by the properties of the host rock, for example, by the intrinsic attenuation, or the properties of the seismic source. Further analyses, which are beyond the scope of this paper, will be required, to further analyze the frequency spectra.

155 4 Travel time tomography

Seismic travel time tomography is a well-established procedure for delineating subsurface structures at various scales (e.g., Nolet (1987)). It requires (i) an initial model, (ii) a forward solver to predict the travel times for a given model, (iii) an inverse solver to estimate the seismic velocities (resp. the seismic slownesses, the inverse of velocity) from the observed data, and (iv) a regularization scheme to account for the underdetermined components of the inverse problem (e.g. Menke (1984)). For our
160 computations, we employed an in-house tomography software that included the algorithm by Podvin and Lecomte (1991) as a forward solver, which solves the Eikonal equation on a regular grid with a finite-difference approach. The seismic rays are then computed with a backtracing algorithm following (Li et al., 2018). The accuracy of the forward solver is governed primarily by the discretization of the finite-difference grid.

To solve the inverse problem, the volume of interest needs to ~~also~~ be discretized in 3D blocks of adequate sizes. In contrast to the forward solver grid, which is governed by the accuracy of the Eikonal solver, the inverse grid is governed by the spatial resolution power offered by the source-receiver distribution. Therefore, the forward and inversion grids do not necessarily have to be identical. The ray segment lengths for each inversion cell and source-receiver pair are determined and fed into the $n \times m$ Jacobian matrix \mathbf{J} , where n is the number of data points and m is the number of inversion cells. Since such
170 tomographic problems always include an underdetermined component, regularization of the inverse problem is required. For

that purpose, we have added damping and smoothing constraints (see Maurer et al. (1998) and Lanz et al. (1998) for further details). The inverse problem can then be written as

$$\begin{pmatrix} \mathbf{J} \\ \mathbf{D} \end{pmatrix} \mathbf{s} = \begin{pmatrix} \mathbf{t} \\ \mathbf{h} \end{pmatrix}, \quad (1)$$

where \mathbf{J} is the Jacobian matrix, \mathbf{t} the observed travel times, \mathbf{D} and \mathbf{h} the regularization constraints, and \mathbf{s} the unknown slownesses. As described, for example, in Maurer et al. (1998), matrix \mathbf{D} is composed of an upper part, including a $m \times m$ diagonal matrix, which is required for the damping constraints, and a lower part, containing an $m \times m$ matrix, representing the smoothing operator. Likewise, the vector of \mathbf{h} contains an upper part with the initial resp. previous slownesses, and a lower part including zeros. The resulting system of equations in 1 is typically very sparse and can thus be solved conveniently with the LSQR algorithm proposed by Paige and Saunders (1982). With the updated velocity model, the predicted travel times and the ray geometry need to be recomputed to update \mathbf{J} . This procedure is then repeated until convergence is achieved.

Since infinitely thin rays, computed with the Eikonal equation, are not a good physical representation of finite-frequency seismic waves, and they often cover not all inversion cells, the concept of fat rays was introduced by Woodward (1992). The underlying idea of this concept is to extend the thin rays to a width that corresponds to the dominant wavelengths of the data observed. When the travel time fields from the solution of the finite-difference Eikonal solver are available, the region of the fat rays can be calculated swiftly with the formula of Červený and Soares (1992) that describe the first Fresnel volume, which is equivalent to the fat ray

$$|t_{sx} + t_{rx} - t_{sr}| \leq T. \quad (2)$$

t_{sx} and t_{rx} are source or receiver travel times to an arbitrary point x within the forward modeling domain, t_{sr} is the predicted travel time with the actual model \mathbf{s} and T is the dominant period of the seismic waves. When the inequality in Equation 2 is satisfied, the point x lies within the fat ray volume. To compute the fat ray volumes, it is necessary to not only solve the forward problem for each source position, but also for each receiver position, which can increase the computational costs significantly. For computing the fat ray Jacobian matrix, it is necessary to compute for every source-receiver pair a function f_x , defined as

$$f_x = \begin{cases} T - t_{sx} - t_{rx} + t_{sr}, & \text{if } |t_{sx} + t_{rx} - t_{sr}| \leq T \\ 0, & \text{otherwise} \end{cases} \quad (3)$$

at every grid point of the forward model. Then, the f_x values, contained in a particular inversion grid cell, are summed up and inserted into the corresponding element of \mathbf{J} . Finally, each row of \mathbf{J} needs to be scaled, such that $\mathbf{J}\mathbf{s} = \mathbf{t}_{sr}$ is enforced.

It is noteworthy that a fat ray approach makes the tomography less dependent on the parameterization of the inversion model. When a relatively fine block discretization is chosen for the inversion model, it becomes likely that numerous blocks are not hit by thin rays. In contrast, fat rays always cover the same volumes, irrespective of the size of the inversion blocks.

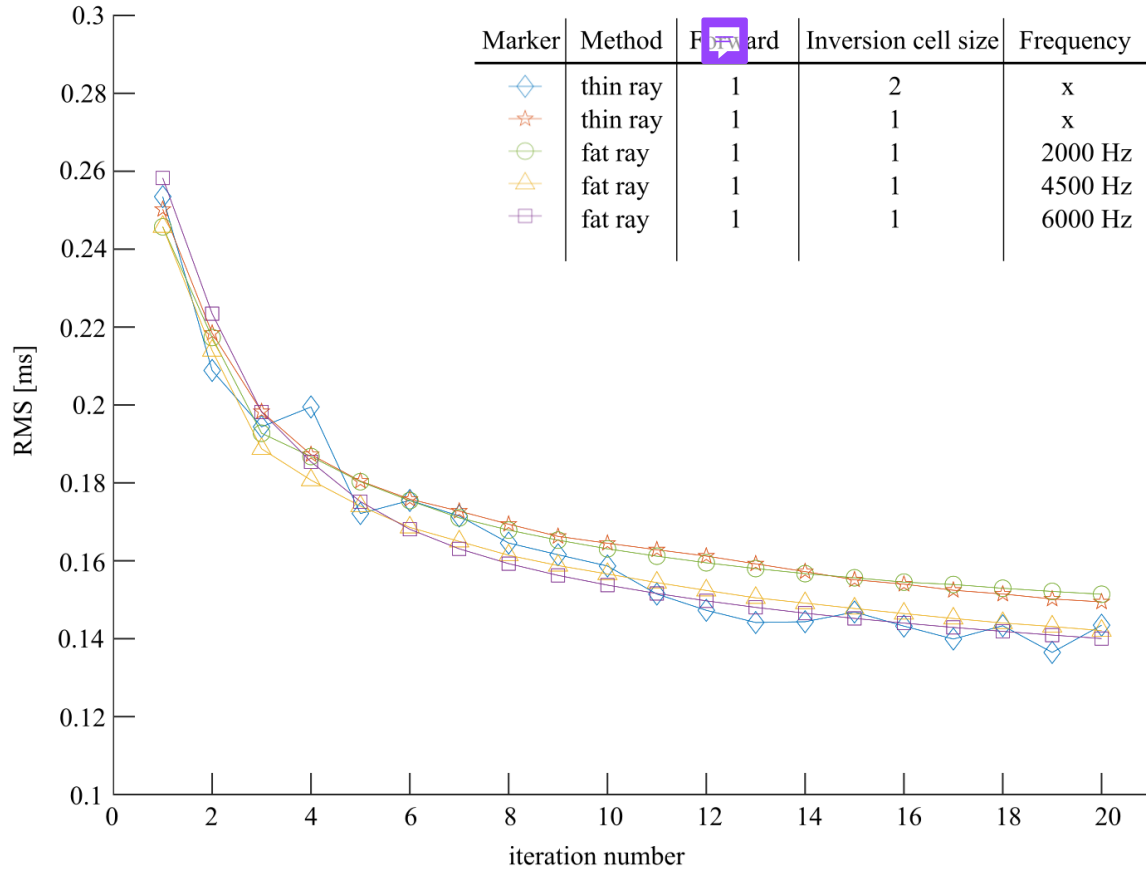


Figure 4. Development of the RMS discrepancy between observed and predicted travel times for different configurations: the thin ray based tomography with two different cell sizes of the inverse solver (1 m and 2 m) and the fat ray tomography with different frequencies, 2 kHz, 4.5 kHz and 6 kHz. Fat ray inversions employed the same grid for the forward solution and inversion $1 \times 1 \times 1 \text{ m}^3$. The same applies to the thin ray 1-1 inversion. For the thin ray 1-2 inversion, 8 forward cells were merged to larger cubic inversion cells.

5 Application to field data set

5.1 Setup of the inversion

For the travel time tomography we used the data presented in Section 3. A homogeneous velocity model of 5300 m/s was used as starting model, estimated from travel time curves of our data. Since the geological observations along the main tunnel and on the borehole cores did not indicate a pronounced layering, we judged a homogeneous initial model to be adequate. The coordinate system was rotated into the main axis system (or principle axis system) of the borehole trajectories to reduce the number of numerical cells. This resulted in a model of dimension of $72 \times 62 \times 406 \text{ m}^3$. We compared different block sizes for

the thin ray-based approach, referred to as "thin ray". The inversion block size was either 2 m or 1 m, but the forward solver
210 block size was always kept at 1 m.

As described in Section 4, we have applied damping and smoothing constraints for the regularization of the inverse problem. The individual contributions of damping and smoothing were determined by trial-and-error. A damping/smoothing ratio of 0.5 proved to be adequate for our setup.

The convergence behavior of the different inversion runs is shown in Figure 4 in the form of Root-Mean-Square discrepancies
215 between observed and predicted travel times (RMS curves). For the fat ray tomography, we always used the smaller inversion cell size of 1 m and compared different frequencies: 2 kHz, 4.5 kHz and 6 kHz that are within the frequency spectra of the P-wave (see Figure 3). With appropriate regularization for the different inversions, all inversion runs converged reasonably well, that is, the RMS curves are flattening out, and they all show a similar convergence behavior. However, for the thin ray inversion with 1 m cell size and for the fat ray inversion with 4.5 kHz and 6 kHz, more regularization was required to account
220 for the larger underdetermined component of the inversion problem (the magnitudes of \mathbf{D} and \mathbf{h} in Equation 1 were increased by 50%). Generally, the RMS reduced from 0.25 ms to approximately 0.15 ms within 20 iterations, which is consistent with our picking accuracy. Since we did not observe significant differences in the convergence behavior of the different settings, and the resulting tomography models were similar, we have chosen 2 kHz for our fat ray tomography to obtain the best spatial coverage with the lowest reasonable frequency.

225 5.2 Comparison of Thin ray and Fat ray tomography

To show the benefit of the fat ray approach, we compare the 2 kHz fat ray results with the thin ray results. For the comparison, we do not only consider the velocity structures, but also the column sums of the Jacobian matrix, subsequently referred to as "coverage", as, for example, described in Jordi et al. (2016). The summation of the j th column of the Jacobian matrix gives an estimate of the overall sensitivity related to the j th inversion cell. The "coverage" measure is similar to the ray-coverage that is
230 often used in thin ray tomography.

In Figure 5, we compare the velocity tomograms for the thin ray (5a) and the 2 kHz fat ray (5b) at a horizontal slice at $z = 150$ m. Additionally, the corresponding coverage plots are shown in Figures 5c) and 5d). Higher velocities are displayed in blue, lower velocities in red, and the mean velocity (≈ 5340 m/s) is represented in gray. Areas with insufficient coverage are shown in white. The green line indicates the MFZ at this depth. Both tomograms show similar features, but the structures in the fat ray
235 tomogram (Figure 5b) are much clearer. Note, for example, the low-velocity anomalies around MB8 and between ST1 and ST2. Furthermore, the area, covered with fat rays, is considerably larger, and it does not include any gaps. Considering the fact that fat rays are a better physical representation of the actual finite frequency wavepaths, one can conclude that the tomogram in Figure 5b is not only clearer, but also likely more reliable.

240 5.3 Qualitative description of the 3D velocity model

In the sequel of the paper, we consider only the velocity model obtained with fat ray tomography using a center frequency of 2 kHz. P-wave velocities in this tomographic model vary between 4685 m/s and 6212 m/s, and the mean velocity is at about 5340 m/s. Figure 6 shows the tomographic velocities in (a) and the corresponding coverage in (b) at different depths. The intersections with the boreholes are shown as black dots (a) and blue dots (b), respectively. The intersection of the slice with the MFZ is marked with a green line.

At $z = 100$ m, we generally observe the highest velocities of all slices. This area is distinguished by largely intact granites (Bröker et al., 2024a). At $z = 150$ m, we observe a low-velocity feature in the region, where the MFZ intersects the slice. At $z = 200$ m and $z = 250$ m, there are several low- and high-velocity zones with moderate amplitudes. The coverage plots in Figure 6b indicate that all the features described are potentially well constrained by the data (see also Appendix A).

A vertical slice through the model is provided in Figure 7. Since the MFZ (see Figure 1) is a feature of major interest, we provide a vertical section perpendicular to the strike of this fault zone through the central part of the 3D model. The vertical section confirms that there are predominantly low velocities between $z = 100$ m to $z = 150$ m, and generally higher velocities are observed at greater depths (see, for example, the region marked with an arrow in Figure 7). Below $z = 250$ m, the coverage and thus the reliability of the velocity model is limited.

The horizontal and vertical slices in Figures 6 and 7 provide some insights into the structure of the 3D velocity model. However, such single slices can be difficult to interpret. Therefore, we have created a series of videos, with which it is possible to scan in various directions through the model cube. They are provided in the digital appendix, and it is highly recommended to make use of them to better understand the structures contained in the 3D model.

The horizontal and vertical slices in Figures 6 and 7 indicate that there are hints of the MFZ (e.g., the low-velocities near the MFZ intersection at $z = 150$ m in Figure 6), but there is no consistent manifestations of it in the 3D velocity. This can either be indicative for a high degree of complexity of the MFZ, but it could also be due to insufficient spatial resolution of the tomograms. To address the latter, we have performed a series of checkerboard tests that are documented in Appendix A. In brief, the tests demonstrated that the spatial resolution lies between 5 and 10 m, with decreased resolution towards the borders of the regions with significant coverage.

5.4 Travel time residuals

To check, how well the 3D tomographic velocity model is capable to explain the observed travel times, we superimpose the observed and predicted travel times in Figure 8a as a function of source-receiver offset. For a better visualization, the travel times t_{eff} are shown in reduced form, that is, $t_{red} = t_{eff} - \Delta/v_{red}$, where Δ is the source-receiver offset and v_{red} is the

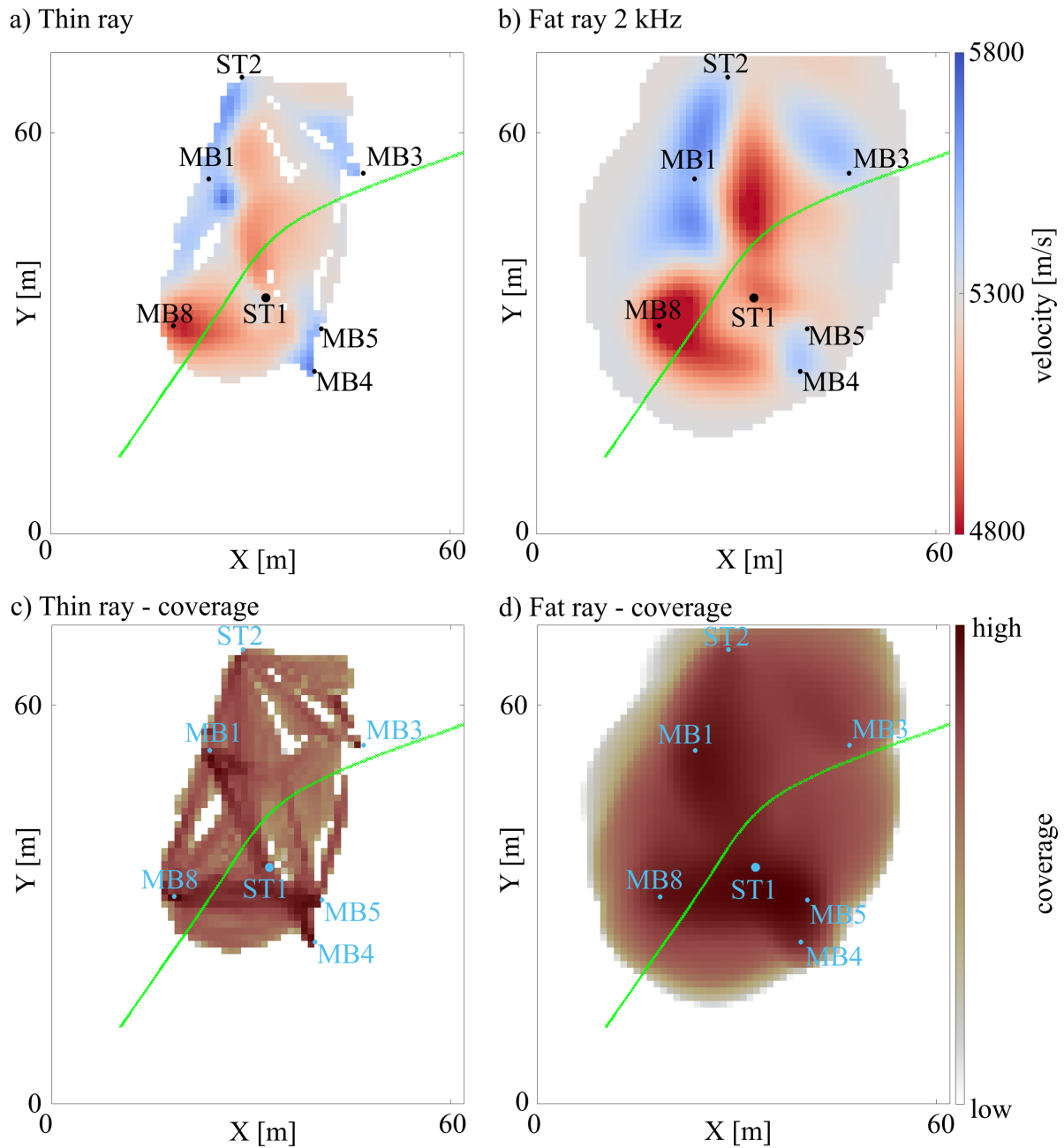


Figure 5. Comparison of thin and fat ray tomography using a x - y slice at $z = 150$ m: a) tomogram of the thin ray approach, (b) tomogram of the 2 kHz fat ray approach. The intersections of the boreholes with the slice are also shown. (c) and (d) show the coverage, defined via the column sums of the Jacobian matrix.

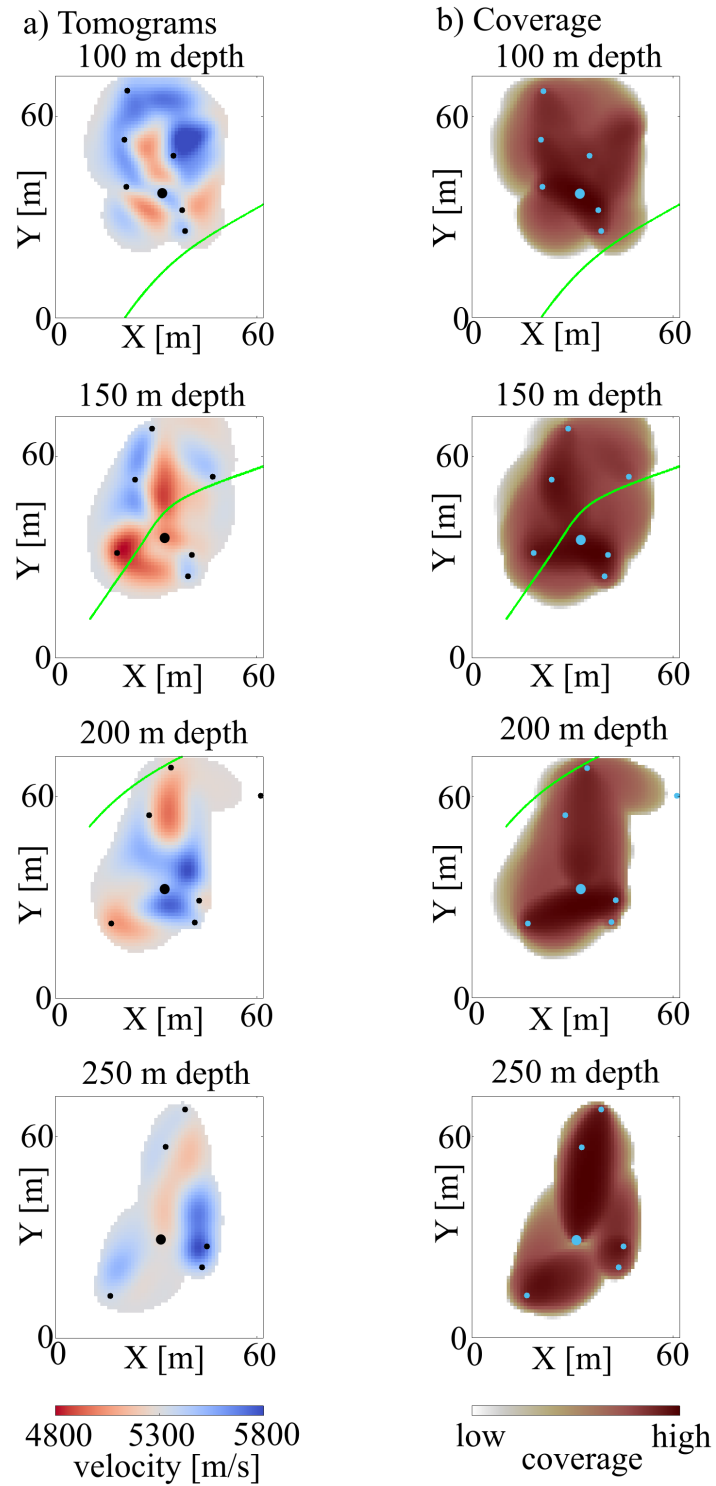


Figure 6. a) Velocity tomograms at different depths and b) the corresponding spatial coverage. Unresolved areas are left white. The dots indicate the intersections of the boreholes with the slice, the larger dot indicates the borehole ST1. The green line indicates the intersection with the MFZ.

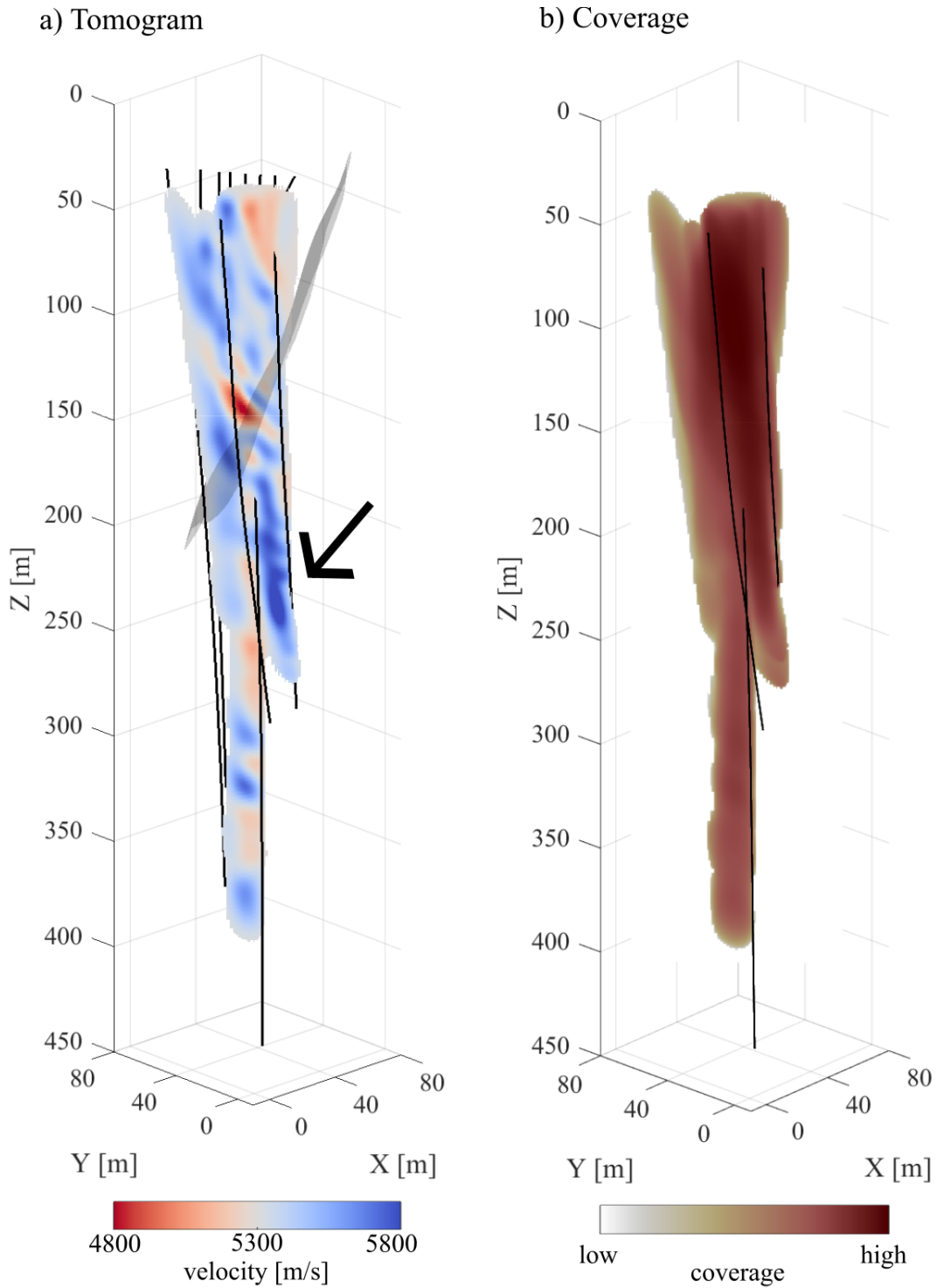


Figure 7. a) Vertical slice perpendicular to the MFZ, which is shown as gray surface. Zone with particularly high velocities is marked with an arrow b) shows the same slice but for the coverage of the model.

reduction velocity, which we have chosen to be 5340 m/s . Consequently, travel times with a ray velocity of v_{red} plot along a horizontal line at $t_{red} = 0$. Additionally, we show the differences between the observed and predicted data (residuals) a function of source-receiver offset (Figure 8b) and in form of a histogram (Figure 8c).

From the residual plots in Figure 8, two main conclusions can be drawn. First, there seem to be no significant offset dependent variations of the residuals (such variations could be indicative for systematic errors in the tomograms). Secondly, about 70% of the residuals are below the average picking accuracy of 0.15 ms (marked with solid black lines in Figures 8b and 8c). Therefore, the standard deviation of the residual distribution is close to the average picking accuracy, thereby indicating that the observed data are neither over- nor under-fitted by the 3D tomographic velocity model.

5.5 Validation of the velocity model with independent data sets

Laboratory measurements at fluid-saturated undisturbed core samples indicated values up to $V_p=5434$ m/s. From these results, P-wave velocities at in-situ conditions with $P_{eff}=15$ MPa were estimated to be 6123 m/s (David et al., 2020). This is broadly consistent with the maximum values observed in the tomograms (6212 m/s).

Another option to validate the velocities obtained by the tomographic inversions is offered by sonic logs, acquired in borehole ST1. A comparison is shown in Figure 9. To compare both data sets, the sonic logs were downsampled to the sampling rate of the tomographic velocity model. The tomographic velocities are shown in black and those from the sonic logs in orange. Adjacent to the velocity profiles, we have also extracted the coverage values along ST1, shown as blue line. They show that the depth range of trustworthy tomographic velocities lies between 50 m and 230 m (denoted by horizontal dashed lines in Figure 9). As a consequence, the tomographic velocities above and below the depth range resolved are close to the initial velocities of 5300 m/s.

In the resolved depth range, the sonic logs show slightly higher velocities compared with the tomographic results. This is expected because the sonic logs employ higher frequencies. Therefore, the comparison with the sonic logs is rather restricted to relative velocity changes. Both curves show a significant low-velocity anomaly at about 150 m depth. To verify this low-velocity zone as a feature of the MFZ, we compare it with ATV (Acoustic Televiwer Log) measurements (Figure 9, right panel) at this depth. We show the ATV travel times, adapted from Bröker et al. (2024a). The ATV measurements reveal a broad fracture zone shown by an increase in ATV travel time up to $180 \mu\text{s}$. Furthermore, Bröker et al. (2024a) provide more evidence on the existence of a significant fracture zone. Spinner, electrical conductivity and temperature logs exhibit very significant anomalies in this depth range. Furthermore, optical televiwer measurements indicate smaller breakouts.

The velocities of the 3D seismic model, extracted along borehole ST1, generally show a good agreement with the borehole logs. So the question arises, if the tomographic velocity model would allow delineations and characterizations further away from the boreholes, where no ground truth information is available. For that purpose, we consider again the horizontal and vertical slices through the 3D velocity model (Figures 6 and 7 and the movies provided in the digital appendix). If the MFZ would

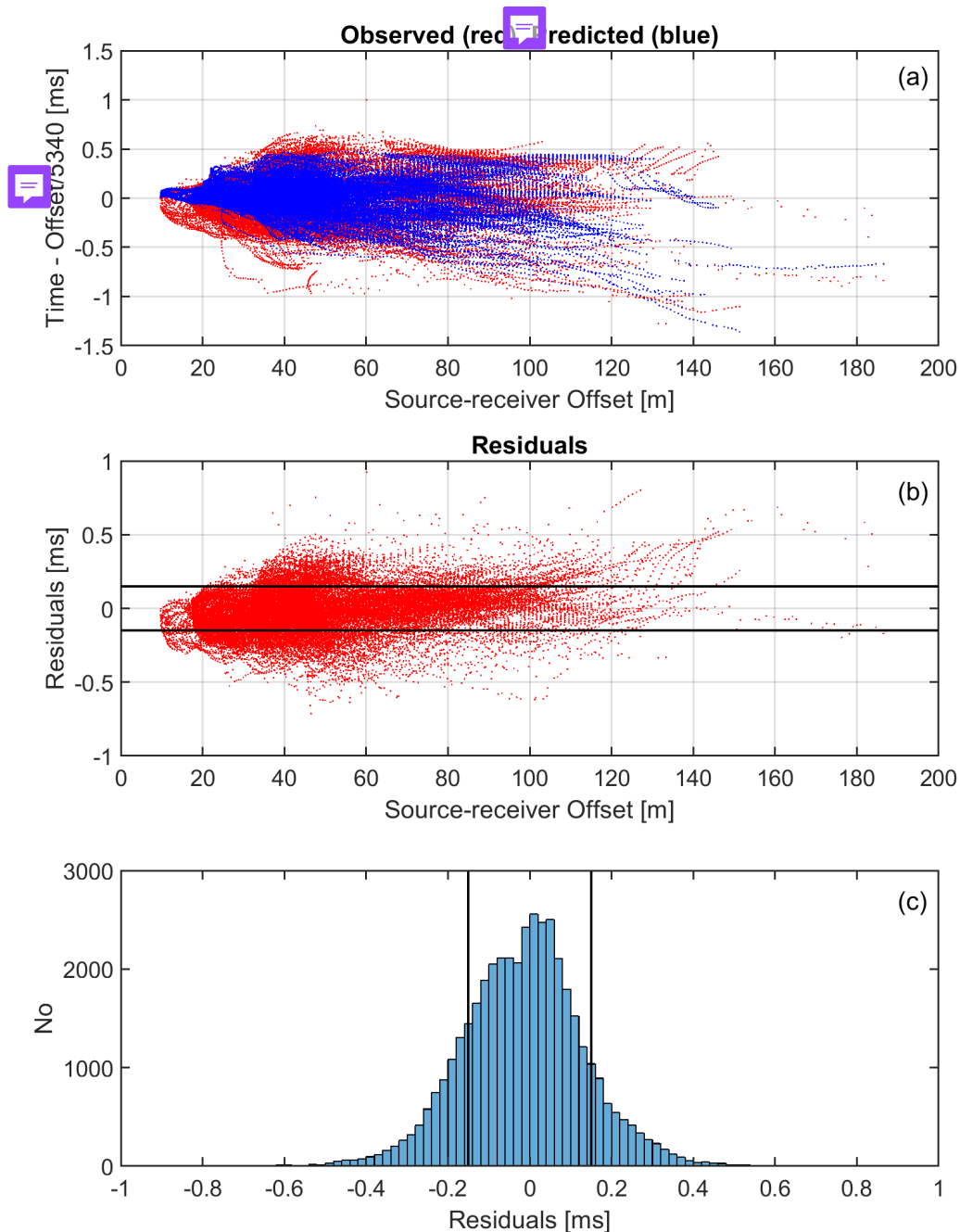


Figure 8. (a) Observed (red) and predicted (blue) travel times as a function of source-receiver offset. (b) Corresponding residuals plotted as a function of source-receiver offset. (c) Residuals shown in form of a histogram. The manually determined picking accuracy is indicated with solid black lines in (b) and (c).

be a clearly confined zone, one would expect a correspondingly well-confined low-velocity zone in the velocity model. Instead, we observe generally decreased velocities along the MFZ intersections, but there is also a substantial amount of heterogeneity. At the ~~horizontal~~ slice at $z = 150$ m (Figure 6), the MFZ is crosscutting the slice in its central part, where the spatial resolution is best, but at $z = 100$ m and $z = 200$ m, the intersection is at the border of the resolution limit (Figure 6b). As demonstrated in Appendix A, the resolving power of our data set is limited towards the edges of the regions with coverage. Therefore, it remains unclear, if the heterogeneities are the result of the complexity of the MFZ, or if they are caused by the limited spatial resolution. Most likely, both effects contribute to the ~~velocity~~ structures ~~observed~~.

5.6 Appraisal of rock quality

The velocity variations found in the tomographic volume are relatively small, and 99% of the velocities lie in the range $4900 < v_p < 5800$ m/s. This is consistent with the findings from borehole logs (Shakas, 2019) that the host rock is moderately disturbed. The velocity variations can be further quantified using the seismic rock quality designation factor (SRQD) introduced by Deere and Miller (1966):

$$SRQD = \left(\frac{v_p}{v_p^{lab}} \right)^2 \times 100. \quad (4)$$

v_p^{lab} is the velocity of the intact rock measured in the laboratory, which is 6123 m/s for the BedrettoLab (David et al., 2020). According to Deere and Deere (1988), the SRQD is a good approximation to the rock quality designation factor (RQD). The SRQD values within our tomographic model lie between 64 and 90, which translates to a rock quality from "fair" to "good/excellent" (~~Deere and Deere, 1988~~). This is consistent with geological observations in the geothermal testbed. Based on tunnel observations and borehole logs, Ma et al. (2022) concluded that the general amount of fracturing in the geothermal testbed is low to moderate.

5.7 Limitations of the tomographic velocity model

For an appropriate interpretation of the structures found in the tomographic 3D model, it is necessary to consider its inherent limitation. First of all, the spatial resolution needs to be considered. It is influenced by the ray coverage within the model and the seismic wavelengths. As shown in Figures 6 and 7, the coverage of the fat rays is generally high and homogeneous. Williamson and Worthington (1993) demonstrated that the spatial resolution scales approximately with the width of the Fresnel zone. For a frequency of 2 kHz and an average source-receiver distance of about 50 m, the width of the Fresnel zone is approximately 10 m, which corresponds quite well with the minimum feature size in the fat ray tomograms. ~~Furthermore~~, this is ~~remarkably~~ consistent with the results of the checkerboard tests documented in Appendix A.

~~Further~~ factors that may limit the reliability of the tomograms include the presence of seismic anisotropy and ~~accuracy~~ of the borehole traces. As indicated earlier, minor anisotropy effects may exist, but we have chosen to employ an isotropic model. Ignoring significant anisotropy effects during an isotropic inversion would result in layered structures with alternating high and low velocities, thereby mimicking anisotropy. We did not spot a pronounced layering in our tomograms.

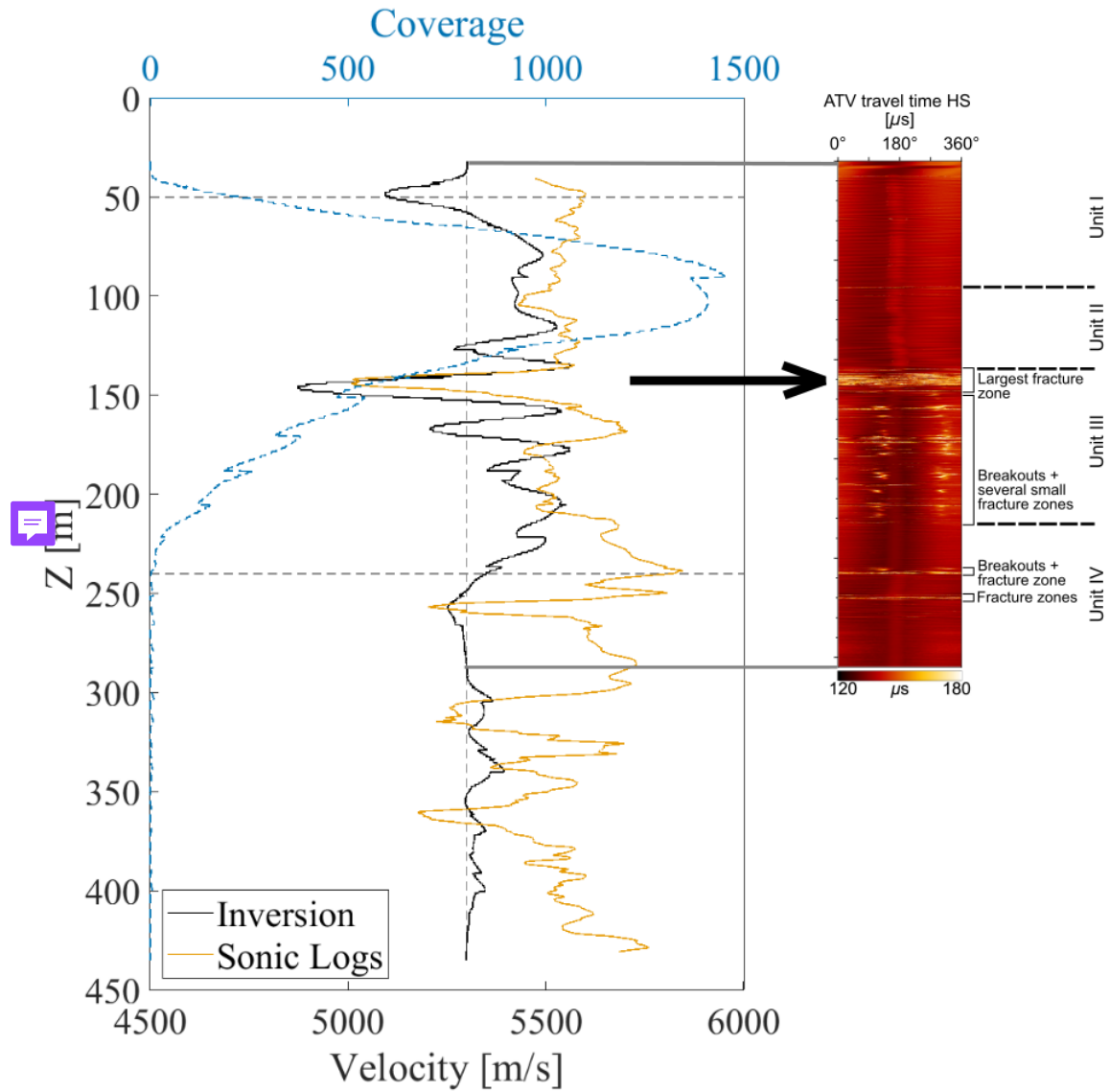


Figure 9. Comparison of the inversion results with additional data acquired along the central borehole ST1 (Figure 1). Tomographic velocities, extracted along ST1 (black) are compared with sonic log data (orange). The horizontal gray dashed lines indicate the zone of significant coverage shown with a dashed blue line (between $z = 50$ m and $z = 250$ m). In this range, we compare the results with ATV logs from Bröker et al. (2024a).

340 Another potential source of systematic errors includes inaccuracies of the borehole trajectories, which tend to increase towards the bottoms of the boreholes. Maurer and Green (1997) has shown that such deviations from the true trajectories would result in substantial anomalies near the borehole bottoms, where the formal resolution is worst and anomalies, caused by systematic errors, ~~can develop most easily~~. Such effects are not observed in our tomograms.

345 Although we can exclude major artifacts from systematic errors, introduced by anisotropy and borehole trajectory inaccuracies, it cannot be excluded that they may have introduced minor distortions. Therefore, only gross features in the tomograms should be interpreted.

5.8 Comparison of seismic velocities with induced seismicity

350 In 2022 - 2023, hydraulic stimulation experiments were conducted in the geothermal testbed by injecting water into selected packer intervals of borehole ST1 (see also Section 2). An overview of these experiments is given in Obermann et al. (2024), with a seismic analysis using DugSeis (Roskopf et al., 2024b, a). We focus here on the seismicity from Phase I, in which eight intervals at depths of $120 < z < 300$ m were stimulated using consistent injection protocols (Bröker et al., 2024a; Doonechaly et al., 2024). We examine the relationship between seismicity and our 3D tomographic velocity model, and assess the effect of
355 velocity heterogeneity on location accuracy.

For the analysis, we selected well-constrained events from the catalog of Obermann et al. (2024), restricted to those within the tomographic model. Events required at least six P-wave picks (no S-wave picks were available) and were relocated using a grid-search algorithm (Moser et al., 1992) with travel times computed via the Eikonal solver (Podvin and Lecomte, 1991)
360 on a 0.5 m grid. Outliers in the pick database were removed using a 0.75 ms threshold, after which the selection criteria were re-applied and events re-relocated. We further excluded events with poor location geometry using the D-criterion (Kijko, 1977; Menke, 1984), adopting a threshold of 1×10^{-7} based on visual inspection. This procedure yielded 4283 events from originally 6413 events for further analysis.

365 All considered events have moment magnitudes $M_w < -3$ and can therefore be attributed to the fluid injections within the geothermal testbed, ~~excluding~~ regional seismicity. Crosshole measurements were performed prior to injection and thus represent pre-stimulation conditions. ~~Since~~ repeated active measurements during stimulation indicated P-wave velocity changes well below 1%, ~~this has negligible impact~~.

5.8.1 Influence of the velocity model on hypocentral parameters

370 Figures 10 and 11 compare event locations obtained with the 3D tomographic model and a homogeneous velocity model with the average velocity of 5340 m/s, both using the same grid search algorithm. Differences are generally small (mean: 2.2 m,

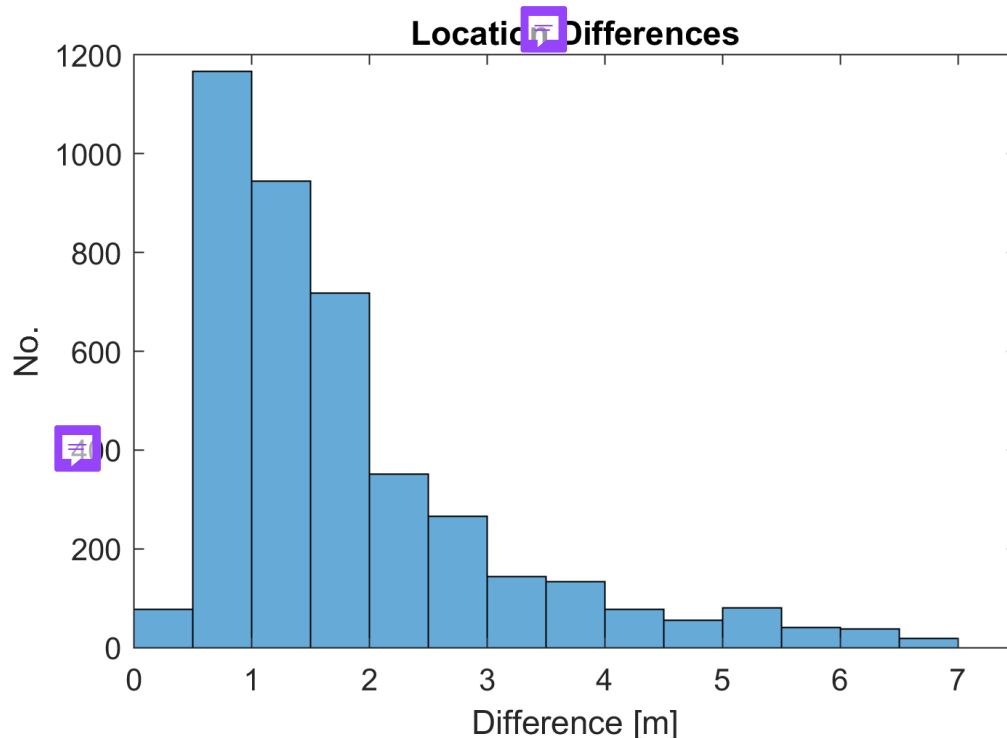


Figure 10. Histogram of the absolute location differences using either a homogeneous or the 3D tomographic model.

median: 1.4 m), with slightly larger deviations at depth $z > 210$ m. No systematic shift is observed between the event locations using the two velocity models. We therefore conclude in line with observations from Roskopf et al. (2024a) that velocity variations in the 3D model have only minor effect on event locations.

375

5.8.2 Spatial correlation of seismic velocities and the induced seismicity

To study the spatial correlation between seismicity and velocity structures, we employed the following methodology. First, we subdivided the velocity model into low-, intermediate and high-velocity regions. Low and high velocities are defined as values more than one standard deviation (≈ 150 m/s) below or above the mean velocity (≈ 5340 m/s). Then, seismic events were superimposed on horizontal and vertical slices of the velocity model, within ± 2.5 m of each slice (Figures 12 and 13; full slice series in the digital appendix).

Several interesting observations can be made in the superimposed images in Figures 12 and 13. In horizontal slices at injection depths seismicity clusters around the injection borehole ST1, with little correlation to the MFZ (green lines in Figure 12). Most events occur in slightly reduced or intermediate velocity zones and only very rarely in high- or very low-velocity

385

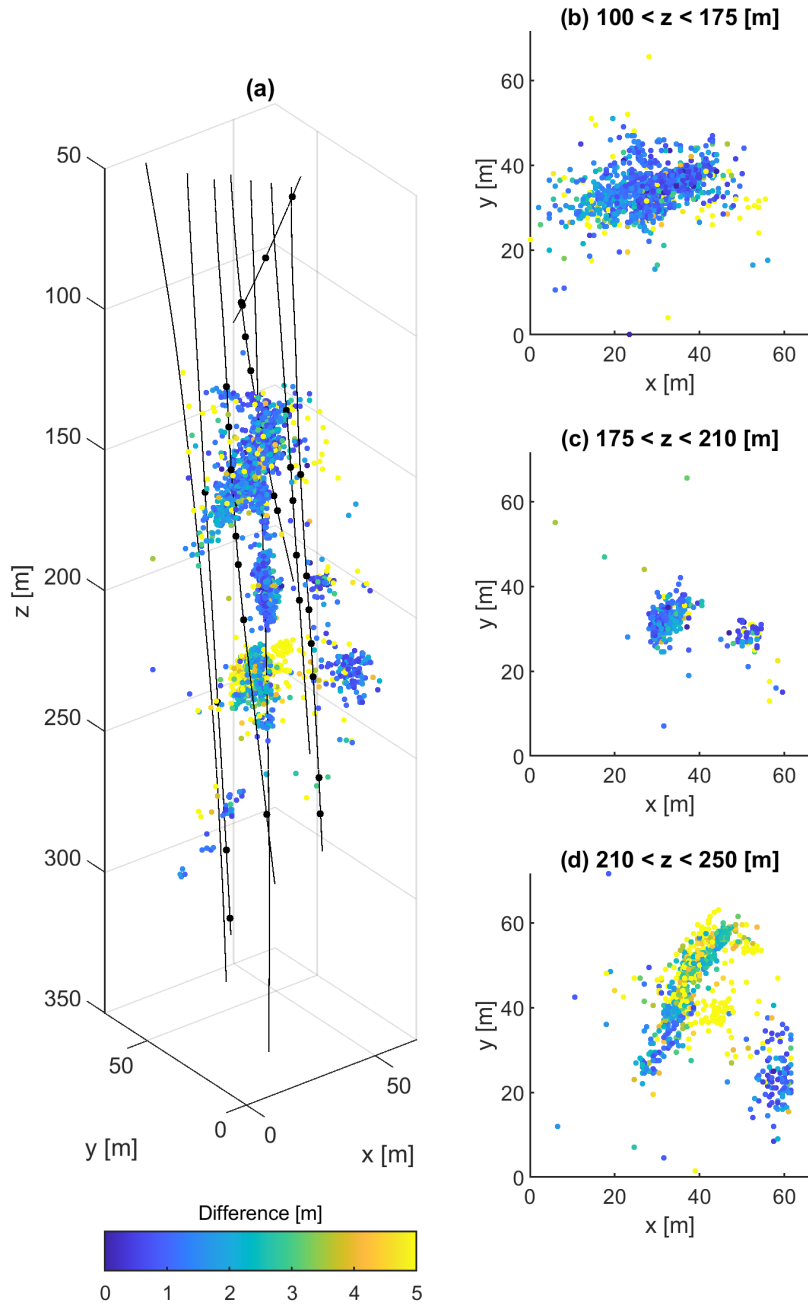


Figure 11. Spatial distribution of location differences shown in Figure 10. Panels (b) to (d) include top view representations of selected depth intervals.

regions. At $z = 237$ m, a distinct cluster lies about 20 m from ST1, almost entirely in the intermediate velocity range. Vertical slices show similar patterns (Figure 13): events are concentrated in slightly reduced or intermediate velocity zones, often along boundaries towards higher-velocity regions.

390 A possible interpretation of these patterns is that high velocities correspond to intact host rock that remained unfractured under injection pressures (< 18 MPa), whereas very low velocities indicate heavily fractured zones incapable of storing sufficient stress. Seismicity thus preferentially occurs in intermediate zones, where fractures exist but rock strength still allows stress accumulation and failure.

395 From a mechanical perspective, seismic velocities reflect stiffness. Microcracking and pore fluids lower velocities and stiffness (e.g., Mavko et al., 2009; Paterson and Wong, 2005), consistent with fault-zone observations (e.g., Faulkner et al., 2010) and laboratory rock-failure experiments (e.g., Stanchits et al., 2011). Velocity contrasts likely create strain gradients and stress concentration at boundaries between intact and damaged rock - a mechanism invoked for acoustic emissions in granite (Salazar Vásquez et al., 2024) and rock bursts in mines (Barton, 2006).

400

A complementary mechanism is fluid migration: lower/intermediate velocity regions are more permeable due to connected microcracks. Fluid preferentially infiltrates these zones, where small pressure perturbations can induce failure if structures are near critical stress (Townend and Zoback, 2000).

405 We finally checked, if similar correlations between seismicity and intermediate velocity zones have been observed at other places ~~and across scales~~. As already mentioned, they were observed in centimeter-scale laboratory tests Salazar Vásquez et al. (2024), and similar observations were made at kilometer-scale geothermal fields (e.g. Hengill, Iceland (Obermann et al., 2022)). Therefore, we conclude that the spatial correlation of seismicity and intermediate velocity zones at the BedrettoLab geothermal testbed is consistent with other observations ~~across scales~~. The most plausible explanations involve stress gradients at
410 velocity contrasts and enhanced permeability in fractured zones. Further work is needed to quantify these mechanisms and link observations with geomechanical processes more directly.

6 Conclusions

The experimental setup of the geothermal testbed in the BedrettoLab offered unique opportunities for 3D tomographic studies. The literature on such investigations on that scale is very sparse - in fact, we could not find a comparable study in the literature.

415 Our finding could thus be a motivation for other experiments in similar environments.

We showed that in comparison with traditional thin ray methods, fat ray tomography does not only better mimic the physics of band-limited seismic data, but it also results in an improved coverage. Furthermore, fat ray tomography is less dependent

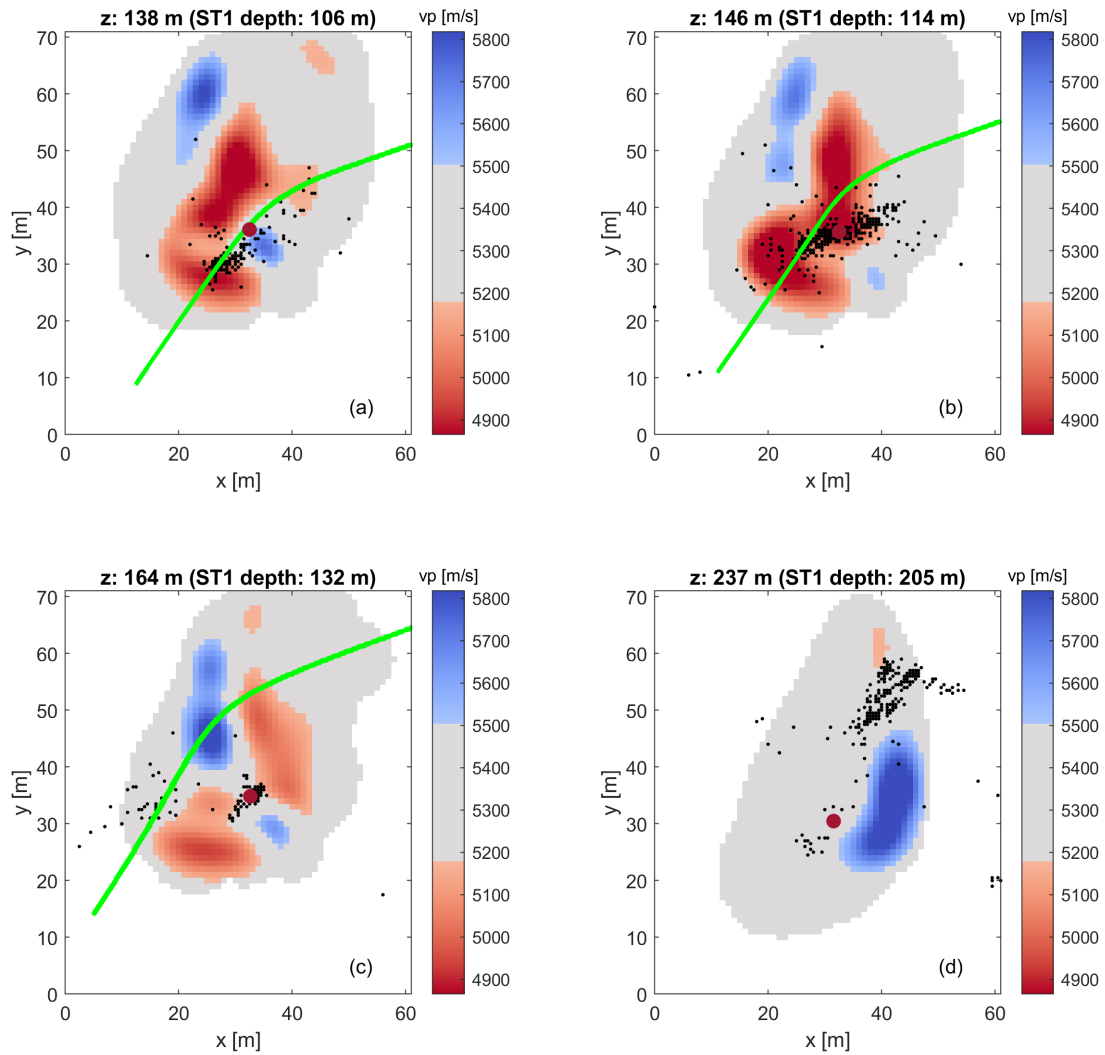


Figure 12. Horizontal slices through the tomographic model. Low and high velocities are shown in red and blue, and intermediate velocity areas are shown gray. The seismicity located ± 2.5 m distance from the slices is superimposed by black dots. The intersection of the MFZ is shown in light green.

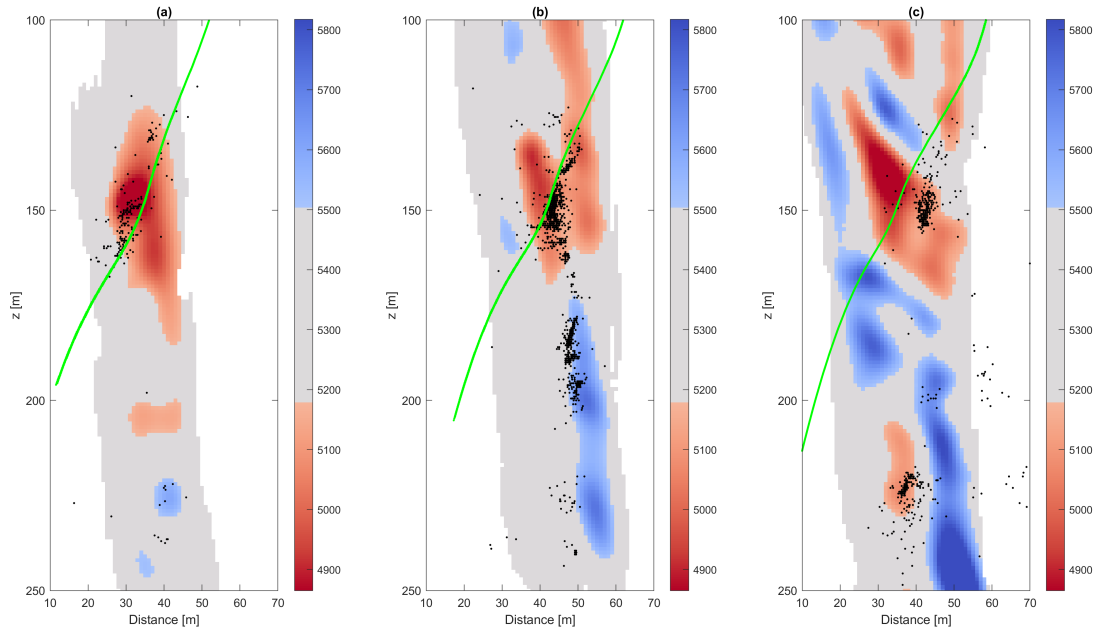


Figure 13. Vertical slices perpendicular to the MFZ through the tomographic model. The slices are located near the trace of the injection borehole ST1 (roughly ± 10 m away from each other). Low and high velocities are shown in red and blue, and intermediate velocity areas are shown gray. The seismicity located ± 2.5 m distance from the slices is superimposed by black dots. The intersection of the MFZ is shown in light green.

on the model parametrization of the inversion grid (compared with thin rays), because the sensitivity kernels (i.e., the fat ray
420 volumes) are unaffected by the discretization of the inversion model.

There are two main findings from the analysis of the 3D velocity model derived with our tomography study. First, we could
characterize a major fault zone. Its signature in the tomographic image is not a narrow and well confined zone of decreased
velocities, as one would expect. Instead, it is distinguished by a relatively large volume of generally decreased velocities with
425 considerable heterogeneities. Checkerboard resolution tests indicated that some of the features may be due to the limited spatial
resolution of our experimental setup, particularly near the boundaries of the region covered by the fat rays.

Secondly, we found a spatial correlation between passive seismic events, generated by hydraulic stimulations, and the velocity
structures in our tomographic model. The induced seismic events occur predominantly between high and very low velocity
430 zones. Based on similar results from a small-scale laboratory study, we attribute this observation to the existence of stress
gradients in the regions of intermediate velocities.

Data availability. The input data for the inversion is published by Maurer and Schwarz (2025): <https://doi.org/10.3929/ethz-b-000725491>. Seismicity catalogs of the VALTER project have been published by Roskopf et al. (2024a)

435 *Video supplement.* Video supplements for the 3D velocity model are published by Maurer and Schwarz (2025) <https://doi.org/10.3929/ethz-b-000725491>

Appendix A: Appendix A: Checkerboard Tests

The spatial resolution of the tomographic inversions is a key information for ~~interpreting the 3D~~ tomograms. There are several options that can be considered for appraising the spatial resolution. For seismic tomography, so-called checkerboard tests established themselves to be a useful tool (e.g., Zelt and Barton, 1998). Although such tests have well-known limitations (e.g.,
440 Leveque et al., 1993; Rawlinson and Spakman, 2016), they can provide a first-order estimate of the spatial resolution.

For checking the resolution ~~power~~ of our data set set, we generated synthetic data with block sizes of $5 \times 5 \times 5 m^3$, $10 \times 10 \times 10 m^3$ and $15 \times 15 \times 15 m^3$. The same source-receiver configurations, as employed for the inversion of the observed data sets, were considered, and the same processing workflows were applied. The results are shown in Figures A1 to A3. They show selected
445 slices through the 3D models. It is evident that block sizes of 15 and 10 metres can be generally well resolved, but structures of the size of 5 meters remain unresolved in most areas. It is also observed that the spatial resolution decreases, as expected, towards the boundaries of the regions ~~covered~~ by rays. This is particularly apparent in the ~~horizontal~~ slices in Figure A3.

Author contributions. MLS performed the data analysis, the Inversion and wrote the paper. HM supervised MLS, performed the earthquake relocation and wrote/edited the paper. AO and AS organized the data acquisition, performed preliminary tests and edited the paper. PAS
450 edited the paper. HM, SW and DG supervised the project.

Competing interests. The authors declare that they have no conflict of interest.

Acknowledgements. In the "Bedretto Underground Laboratory for Geosciences and Geoenergies", ETH Zurich studies in close collaboration with national and international partners techniques and procedures for a safe, efficient, and sustainable use of geothermal heat and questions related to earthquake physics. The BedrettoLab is financed by the Werner Siemens Foundation, ETH Zürich and the Swiss National Science
455 Foundation. Miriam Schwarz is funded by the SNF Multi PhD (200021_192151) project. The research in this publication has received additional funding by the project VALTER (Validierung von Technologien zur Reservoir Entwicklung) (SI/501496-01). The BedrettoLab would like to thank Matterhorn Gotthard Bahn for providing access to the tunnel. We would like to thank Kai Bröker for his feedback on

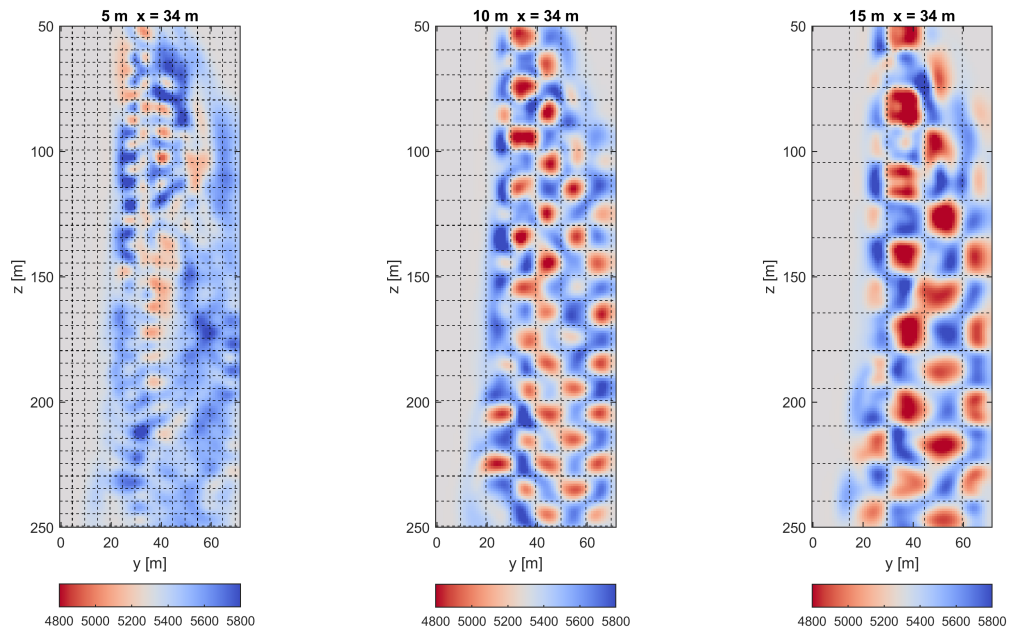


Figure A1. Vertical cross section along a y-z slice at $x = 34$ m. The dashed lines indicate the locations and size of the checkerboard blocks. Block sizes are 5 (left), 10 (middle) and 15 (right) metres.

section 2, particularly regarding fracture mapping in the BedrettoLab. We thank the BedrettoLab Operation Team, led by Marian Herrich, for their excellent support, which was essential for this project. This paper is BULGG publication BPN_029

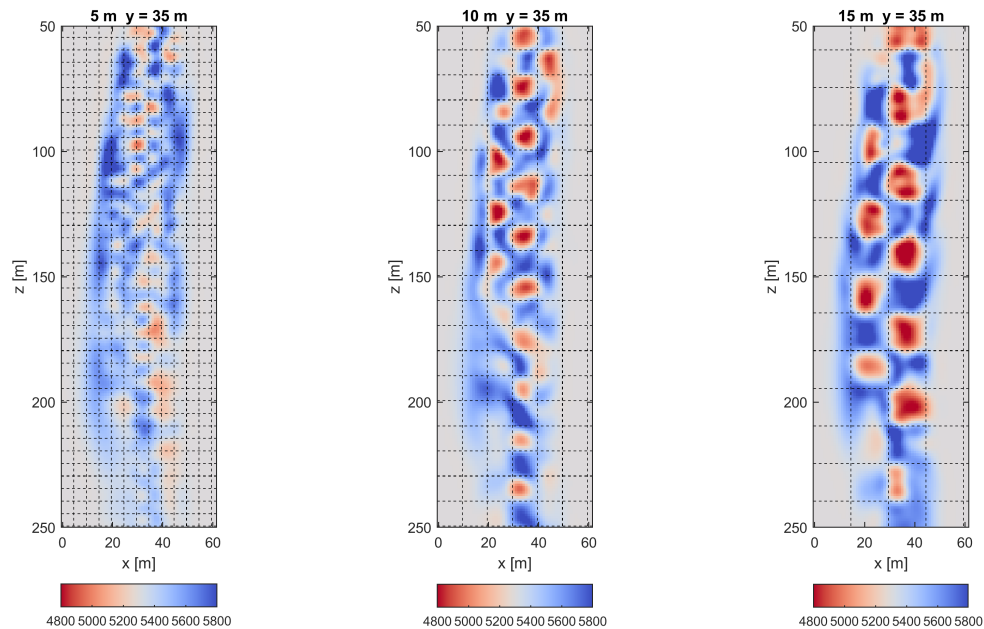


Figure A2. Vertical cross section along a x-z slice at $y = 35$ m. The dashed lines lines indicate the locations and size of the checkerboard blocks. Block sizes are 5 (left), 10 (middle) and 15 (right) metres.

460 References

- Amann, F., Gischig, V., Evans, K., Doetsch, J., Jalali, R., Valley, B., Krietsch, H., Dutler, N., Villiger, L., Brixel, B., Klepikova, M., Kitzilä, A., Madonna, C., Wiemer, S., Saar, M. O., Loew, S., Driesner, T., Maurer, H., and Giardini, D.: The seismo-hydromechanical behavior during deep geothermal reservoir stimulations: Open questions tackled in a decameter-scale in situ stimulation experiment, <https://doi.org/10.5194/se-9-115-2018>, 2018.
- 465 Barton, N.: Rock Quality, Seismic Velocity, Attenuation and Anisotropy, CRC Press, ISBN 9781134160136, <https://doi.org/10.1201/9780203964453>, 2006.
- Behnen, K., Hertrich, M., Maurer, H., Shakas, A., Bröker, K., Epiney, C., Blanch Jover, M., and Giardini, D.: Investigation of Seismic Anisotropy in the Undisturbed Rotondo Granite, <https://doi.org/10.5194/egusphere-2024-1919>, 2024.
- Block, L. V., Cheng, C. H., Fehler, M. C., and Phillips, W. S.: Seismic imaging using microearthquakes induced by hydraulic fracturing, *Geophysics*, 59, 102–112, <https://doi.org/10.1190/geo1992-0156>, 1994.
- 470 Bröker, K., Ma, X., Gholizadeh Doonechaly, N., Rosskopf, M., Obermann, A., Rinaldi, A. P., Hertrich, M., Serbeto, F., Maurer, H., Wiemer, S., and Giardini, D.: Hydromechanical characterization of a fractured crystalline rock volume during multi-stage hydraulic stimulations at the BedrettoLab, *Geothermics*, 124, <https://doi.org/10.1016/j.geothermics.2024.103126>, 2024a.

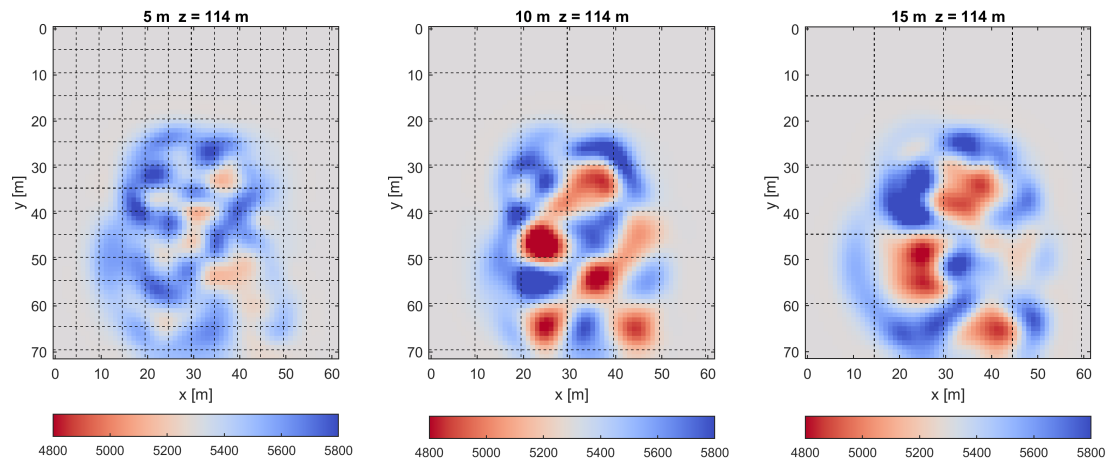


Figure A3. Horizontal cross section along a slice at $z = 114$ m. The dashed lines lines indicate the locations and size of the checkerboard blocks. Block sizes are 5 (left), 10 (middle) and 15 (right) metres.

- Bröker, K., Ma, X., Zhang, S., Doonechaly, N. G., Hertrich, M., Klee, G., Greenwood, A., Caspari, E., and Giardini, D.: Constraining the
 475 stress field and its variability at the BedrettoLab: Elaborated hydraulic fracture trace analysis, *International Journal of Rock Mechanics and Mining Sciences*, 178, 105 739, <https://doi.org/https://doi.org/10.1016/j.ijrmms.2024.105739>, 2024b.
- Ceccato, A., Behr, W. M., Zappone, A. S., Tavazzani, L., and Giuliani, A.: Structural Evolution, Exhumation Rates, and Rheology of the European Crust During Alpine Collision: Constraints From the Rotondo Granite—Gotthard Nappe, *Tectonics*, 43, <https://doi.org/10.1029/2023TC008219>, 2024.
- 480 Červený, V. and Soares, J. E. P.: Fresnel volume ray tracing, *GEOPHYSICS*, 57, 902–915, <https://doi.org/10.1190/1.1443303>, 1992.
- Charlétý, J., Cuenot, N., Dorbath, C., and Dorbath, L.: Tomographic study of the seismic velocity at the Soultz-sous-Forêts EGS/HDR site, *Geothermics*, 35, 532–543, <https://doi.org/10.1016/j.geothermics.2006.10.002>, 2006.
- David, C., Nejati, M., and Geremia, D.: On petrophysical and geomechanical properties of Bedretto Granite, Tech. rep., <https://doi.org/...>, 2020.
- 485 Deere, D. and Deere, D.: The Rock Quality Designation (RQD) in Practice, *Rock Classification Systems for Engineering Purposes*, ASTM STP 984, pp. 91–101, 1988.
- Deere, D. and Miller, R.: *Classification and index properties of intact roc*, New Mexico, 1966.

- Diehl, T., Cauzzi, C., Clinton, J., Kraft, T., Kästli, P., Massin, F., Lanza, F., Simon, V., Grigoli, F., Hobiger, M., Roth, P., Haslinger, F., Fäh, D., and Wiemer, S.: Earthquakes in Switzerland and surrounding regions during 2019 and 2020, *Swiss Journal of Geosciences*, 118, 490 <https://doi.org/10.1186/s00015-025-00489-4>, 2025.
- Doonechaly, N. G., Bröker, K., Hertrich, M., Rosskopf, M., Obermann, A., Durand, V., Serbeto, F., Shakas, A., Ma, X., Rinaldi, A. P., Repollés, V. C., Villiger, L., Meier, M.-A., Gischig, V., Plenkers, K., Maurer, H., Wiemer, S., and Giardini, D.: Insights from Subsurface Monitoring for Engineering of the Stimulation Pattern in Fractured Reservoirs, <https://doi.org/10.21203/rs.3.rs-4859925/v1>, 2024.
- Edwards, B., Kraft, T., Cauzzi, C., Kästli, P., and Wiemer, S.: Seismic monitoring and analysis of deep geothermal projects in St. Gallen and Basel, Switzerland, *Geophysical Journal International*, 201, 1022–1039, <https://doi.org/10.1093/gji/ggv059>, 2015.
- Ellsworth, W. L., Giardini, D., Townend, J., Ge, S., and Shimamoto, T.: Triggering of the Pohang, Korea, Earthquake (Mw 5.5) by enhanced geothermal system stimulation, <https://doi.org/10.1785/0220190102>, 2019.
- Escallon, D., Shakas, A., and Maurer, H.: Modelling and inferring fracture curvature from borehole GPR data: A case study from the Bedretto Laboratory, Switzerland, *Near Surface Geophysics*, 22, 235–254, <https://doi.org/10.1002/nsg.12286>, 2024.
- 500 Faulkner, D. R., Jackson, C. A., Lunn, R. J., Schlische, R. W., Shipton, Z. K., Wibberley, C. A., and Withjack, M. O.: A review of recent developments concerning the structure, mechanics and fluid flow properties of fault zones, <https://doi.org/10.1016/j.jsg.2010.06.009>, 2010.
- Gischig, V. S., Giardini, D., Amann, F., Hertrich, M., Krietsch, H., Loew, S., Maurer, H., Villiger, L., Wiemer, S., Bethmann, F., Brixel, B., Doetsch, J., Doonechaly, N. G., Driesner, T., Dutler, N., Evans, K. F., Jalali, M., Jordan, D., Kittilä, A., Ma, X., Meier, P., Nejati, M., Obermann, A., Plenkers, K., Saar, M. O., Shakas, A., and Valley, B.: Hydraulic stimulation and fluid circulation experiments in 505 underground laboratories: Stepping up the scale towards engineered geothermal systems, *Geomechanics for Energy and the Environment*, 24, <https://doi.org/10.1016/j.gete.2019.100175>, 2020.
- Heidbach, O., Rajabi, M., Cui, X., Fuchs, K., Müller, B., Reinecker, J., Reiter, K., Tingay, M., Wenzel, F., Xie, F., Ziegler, M. O., Zoback, M. L., and Zoback, M.: The World Stress Map database release 2016: Crustal stress pattern across scales, <https://doi.org/10.1016/j.tecto.2018.07.007>, 2018.
- 510 Heincke, B., Maurer, H., Green, A. G., Willenberg, H., Spillmann, T., and Burlini, L.: Characterizing an unstable mountain slope using shallow 2D and 3D seismic tomography, *Geophysics*, 71, <https://doi.org/10.1190/1.2338823>, 2006.
- Hirschberg, S., Wiemer, S., and Burgherr, P. e.: Energy from the earth Deep geothermal as a resource for the future?, TA-SWISS, 2015, <https://doi.org/10.3929/ethz-a-010277690>, 2015.
- Holliger, K., Musil, M., and Maurer, H. R.: Ray-based amplitude tomography for crosshole georadar data: a numerical assessment, *Tech. rep.*, www.elsevier.com/locate/jappgeo, 2001.
- 515 Husen, S. and Kissling, E.: Local earthquake tomography between rays and waves: fast ray tomography, *Tech. rep.*, ISBN 00319201/01, 2001.
- Jordan, D.: Geological Characterization of the Bedretto Underground Laboratory for Geoenergies, ETH Zurich Research Collection, <https://doi.org/10.3929/ethz-b-000379305>, 2019.
- Jordi, C., Schmelzbach, C., and Greenhalgh, S.: Frequency-dependent traveltimes tomography using fast rays: application to near-surface 520 seismic imaging, *Journal of Applied Geophysics*, 131, 202–213, <https://doi.org/10.1016/j.jappgeo.2016.06.002>, 2016.
- Kijko, A.: An Algorithm for the Optimum Distribution of a Regional Seismic Network-I, *Pageoph*, 115, 999–1009, 1977.
- Kneafsey, T., Dobson, P., Blankenship, D., Schwing, P., White, M., Morris, J. P., Huang, L., Johnson, T., Burghardt, J., Mattson, E., Neupane, G., Strickland, C., Knox, H., Vermuel, V., Ajo-Franklin, J., Fu, P., Roggenthen, W., Doe, T., Schoenball, M., Hopp, C., Tribaldos, V. R., Ingraham, M., Guglielmi, Y., Ulrich, C., Wood, T., Frash, L., Pyatina, T., Vandine, G., Smith, M., Horne, R., McClure, M., Singh, A.,

- 525 Weers, J., and Robertson, M.: The EGS Collab project: Outcomes and lessons learned from hydraulic fracture stimulations in crystalline rock at 1.25 and 1.5 km depth, *Geothermics*, 126, <https://doi.org/10.1016/j.geothermics.2024.103178>, 2025.
- Labhart T: Erläuterungen Zum Geologischen Atlas Des Schweiz 1:25000, Val Bedretto, 2005.
- Lanz, E., Maurer, H., and Green, A. G.: Refraction tomography over a buried waste disposal site, *Geophysics*, 63, 1414–1433, <https://doi.org/10.1190/1.1444443>, 1998.
- 530 Leveque, J.-J., Rivera, L., and Wittlinger, G.: On the use of the checker-board test to assess the resolution of tomographic inversions, <https://academic.oup.com/gji/article/115/1/313/604170>, 1993.
- Li, B., Ding, L., Hu, D., and Zheng, S.: Backtracking Algorithm-based Disassembly Sequence Planning, in: *Procedia CIRP*, vol. 69, pp. 932–937, Elsevier B.V., ISSN 22128271, <https://doi.org/10.1016/j.procir.2017.12.007>, 2018.
- Lützenkirchen, V. and Loew, S.: Late Alpine brittle faulting in the Rotondo granite (Switzerland): Deformation mechanisms and fault evolution, *Swiss Journal of Geosciences*, 104, 31–54, <https://doi.org/10.1007/s00015-010-0050-0>, 2011.
- 535 Ma, X., Hertrich, M., Amann, F., Bröker, K., Doonechaly, N. G., Gischig, V., Hochreutener, R., Kästli, P., Krietsch, H., Marti, M., Nägeli, B., Nejati, M., Obermann, A., Plenkers, K., Rinaldi, A. P., Shakas, A., Villiger, L., Wenning, Q., Zappone, A., Bethmann, F., Castilla, R., Seberto, F., Meier, P., Driesner, T., Loew, S., Maurer, H., Saar, M. O., Wiemer, S., and Giardini, D.: Multi-disciplinary characterizations of the BedrettoLab-A new underground geoscience research facility, *Solid Earth*, 13, 301–322, <https://doi.org/10.5194/se-13-301-2022>,
- 540 2022.
- Maurer, H. and Green, A. G.: Potential coordinate mislocations in crosshole tomography: Results from the Grimsel test site, Switzerland, *Tech. Rep. 6*, <http://pubs.geoscienceworld.org/geophysics/article-pdf/62/6/1696/3172949/1696.pdf>, 1997.
- Maurer, H. and Schwarz, M. L.: Data collection to: New insights on the fault structure of a geothermal testbed and the associated seismicity based on active seismic tomography, <https://doi.org/10.3929/ETHZ-B-000725491>, 2025.
- 545 Maurer, H., Holliger, K., and Boerner, D. E.: Stochastic regularization: Smoothness or similarity?, *Geophysical Research Letters*, 25, 2889–2892, <https://doi.org/10.1029/98GL02183>, 1998.
- Mavko, G., Mukerji, T., and Dvorkin, J.: *The Rock Physics Handbook*, Cambridge University Press, 2nd edition edn., ISBN 9780521861366, <https://doi.org/10.1017/CBO9780511626753>, 2009.
- Meier, M.: Geological characterisation of an underground research facility in the Bedretto tunnel, *ETH Zurich Research Collection*, <https://doi.org/10.3929/ethz-b-000334001>, 2017.
- 550 Menke, W.: *Geophysical Data Analysis: Discrete Inverse Theory*, Elsevier, ISBN 9780124909205, <https://doi.org/10.1016/B978-0-12-490920-5.X5001-7>, 1984.
- Moser, T. J., Van Eck, T., and Nolet, G.: Hypocenter determination in strongly heterogeneous Earth models using the shortest path method, *Journal of Geophysical Research*, 97, 6563–6572, <https://doi.org/10.1029/91JB03176>, 1992.
- 555 Nakagome, O., Uchida, T., and Horikoshi, T.: Seismic reflection and VSP in the kakkonda geothermal field, japan: fractured reservoir characterization, *Geothermics*, 27, 535–552, [https://doi.org/10.1016/S0375-6505\(98\)00032-7](https://doi.org/10.1016/S0375-6505(98)00032-7), 1998.
- Nakata, N., Vasco, D. W., Shi, P., Bai, T., Lanza, F., Dyer, B., Chen, C., Park, S.-E., and Qiu, H.: Elastic Characterization at Utah FORGE: P-wave Tomography and VSP Subsurface Imaging, *Tech. rep.*, 2023.
- Nolet, G.: *Seismic Tomography*, Springer Netherlands, Dordrecht, ISBN 978-90-277-2583-7, <https://doi.org/10.1007/978-94-009-3899-1>,
- 560 1987.
- Obermann, A. and Hillers, G.: Seismic time-lapse interferometry across scales, in: *Advances in Geophysics*, vol. 60, pp. 65–143, Academic Press Inc., ISBN 9780128175484, <https://doi.org/10.1016/bs.agph.2019.06.001>, 2019.

- Obermann, A., Wu, S. M., Ágústsdóttir, T., Duran, A., Diehl, T., Sánchez-Pastor, P., Kristjansdóttir, S., Hjörleifsdóttir, V., Wiemer, S., and Hersir, G. P.: Seismicity and 3-D body-wave velocity models across the Hengill geothermal area, SW Iceland, *Frontiers in Earth Science*, 10, <https://doi.org/10.3389/feart.2022.969836>, 2022.
- Obermann, A., Roskopf, M., Plenkers, K., Broeker, K., Rinaldi, A., Doonechaly, N., Gischig, V., Zappone, A., Amann, F., Cocco, M., Hertrich, M., Jalali, M., Junker, J., Kästli, P., Ma, X., Maurer, H., Meier, M.-A., Schwarz, M., Selvadurai, P., and Giardini, D.: Seismic response of hectometer-scale fracture systems to hydraulic stimulation in the Bedretto Underground laboratory, Switzerland, *Journal of Geophysical Research: Solid Earth*, <https://doi.org/10.1029/2024JB029836>, 2024.
- Olasolo, P., Juárez, M. C., Morales, M. P., Damico, S., and Liarte, I. A.: Enhanced geothermal systems (EGS): A review, <https://doi.org/10.1016/j.rser.2015.11.031>, 2016.
- Paige, C. C. and Saunders, M. A.: LSQR: An Algorithm for Sparse Linear Equations and Sparse Least Squares, pp. 43–71, 1982.
- Paterson, M. S. and Wong, T.-f.: *Experimental Rock Deformation – The Brittle Field*, Springer-Verlag Berlin Heidelberg 2005, second edition edn., ISBN 978-3-540-24023-5, 2005.
- Place, J., Sausse, J., Marthelot, J. M., Diraison, M., Géraud, Y., and Naville, C.: 3-D mapping of permeable structures affecting a deep granite basement using isotropic 3C VSP data, *Geophysical Journal International*, 186, 245–263, <https://doi.org/10.1111/j.1365-246X.2011.05012.x>, 2011.
- Plenkers, K., Manthei, G., and Kwiatak, G.: Underground In-situ Acoustic Emission in Study of Rock Stability and Earthquake Physics, in: *Springer Tracts in Civil Engineering*, pp. 403–476, Springer Science and Business Media Deutschland GmbH, https://doi.org/10.1007/978-3-030-67936-1_16, 2022.
- Podvin, P. and Lecomte, I.: Finite difference computation of traveltimes in very contrasted velocity models: a massively parallel approach and its associated tools, Tech. rep., <https://academic.oup.com/gji/article/105/1/271/671376>, 1991.
- Pratt, R. G. and Worthington, M. H.: The application of diffraction tomography to cross-hole seismic data, *Geophysics*, 53, 1284–1294, <https://doi.org/10.1190/1.1442406>, 1988.
- Rast, M., Galli, A., Ruh, J. B., Guillong, M., and Madonna, C.: Geology along the Bedretto tunnel: kinematic and geochronological constraints on the evolution of the Gotthard Massif (Central Alps), *Swiss Journal of Geosciences*, 115, <https://doi.org/10.1186/s00015-022-00409-w>, 2022.
- Rawlinson, N. and Spakman, W.: On the use of sensitivity tests in seismic tomography, *Geophysical Journal International*, 205, 1221–1243, <https://doi.org/10.1093/gji/ggw084>, 2016.
- Roskopf, M., Durand, V., Plenkers, K., Villiger, L., Giardini, D., and Obermann, A.: Accuracy of picoseismic catalogs in hectometer-scale in-situ experiments, <https://doi.org/10.22541/essoar.172736342.25689581/v1>, 2024a.
- Roskopf, M., Durand, V., Villiger, L., and Doetsch, J.: DUGseis: A Python package for real-time and post-processing of picoseismicity, <https://doi.org/10.21105/joss.06768i>, 2024b.
- Salazar Vásquez, A. F., Selvadurai, P. A., Bianchi, P., Madonna, C., Germanovich, L. N., Puzrin, A. M., Wiemer, S., Giardini, D., and Rabaiotti, C.: Aseismic strain localization prior to failure and associated seismicity in crystalline rock, *Scientific Reports*, 14, <https://doi.org/10.1038/s41598-024-75942-9>, 2024.
- Sergeev, S. A., Meier, M., and Steiger, R. H.: EPSL Improving the resolution of single-grain U/Pb dating by use of zircon extracted from feldspar: Application to the Variscan magmatic cycle in the central Alps, Tech. rep., 1995.
- Shakas, A.: *Borehole Logging Data from Characterization Boreholes in Bedretto Underground Lab for Geoenergies*, 2019.

- 600 Stanchits, S., Mayr, S., Shapiro, S., and Dresen, G.: Fracturing of porous rock induced by fluid injection, *Tectonophysics*, 503, 129–145, <https://doi.org/10.1016/j.tecto.2010.09.022>, 2011.
- Townend, J. and Zoback, M. D.: How faulting keeps the crust strong, *GEOLOGY*, 28, 399–402, 2000.
- Williamson, P. R. and Worthington, M. H.: Resolution limits in ray tomography due to wave behavior: numerical experiments, *Geophysics*, 58, 727–735, <https://doi.org/10.1190/1.1443457>, 1993.
- 605 Woodward, M. J.: Wave-equation tomography, *Geophysics*, 57, 15–26, <https://doi.org/10.1190/1.1443179>, 1992.
- Zang, A., Niemz, P., Specht, S. V., Zimmermann, G., Milkereit, C., Plenkers, K., and Klee, G.: Comprehensive data set of in situ hydraulic stimulation experiments for geothermal purposes at the Äspö Hard Rock Laboratory (Sweden), *Earth System Science Data*, 16, 295–310, <https://doi.org/10.5194/essd-16-295-2024>, 2024.
- Zelt, C. A. and Barton, P. J.: Three-dimensional seismic refraction tomography: A comparison of two methods applied to data from the
- 610 Faeroe Basin, <https://doi.org/10.1029/97jb03536>, 1998.